FINITE ELEMENT MICROMECHANICS MODELS
FOR PREDICTING STIFFNESS AND STRENGTH
OF TEXTILE COMPOSITE MATERIALS

By

RAMESH V. MARREY

A DISSERTATION PRESENTED TO THE GRADUATE SCHOOL
OF THE UNIVERSITY OF FLORIDA IN PARTIAL FULFILLMENT
OF THE REQUIREMENTS FOR THE DEGREE OF
DOCTOR OF PHILOSOPHY

UNIVERSITY OF FLORIDA

1995

ACKNOWLEDGEMENTS

TABLE OF CONTENTS

FINITE ELEMENT MICROMECHANICS MODELS FOR PREDICTING
STIFFNESS AND STRENGTH OF TEXTILE COMPOSITE MATERIALS

By

Ramesh V. Marrey

August, 1995

The objective of this study is to develop micromechanical models for predicting the
stiffness and strength properties of textile composite materials. Micromechanical analysis
of textile composites is possible due to the presence of a repeating unit-cell or representative
volume element. The unit-cell is assumed to span the material continuously in all three
dimensions. On the microscale—comparable to the scale of the unit-cell—the composite is
heterogeneous due to the presence of the reinforcing yarn and the matrix. However, on the
macroscale—comparable to the structural scale—the composite is assumed to be
homogeneous and orthotropic. The homogeneous composite properties are then predicted
from the constituent material properties and the yarn geometry.

The highlight of this study is a systematic analysis of issues involved in the finite
element based micromechanics of textile composites. The unit-cell is discretized with
three-dimensional finite elements, and periodic boundary conditions are imposed between
opposite end-faces of the unit-cell. Six linearly independent deformations are applied to the
unit-cell. From the forces acting on the unit-cell for each of the six deformations, the

composite stiffness matrix is obtained. A similar procedure is followed to determine the composite coefficients of thermal expansion. The numerical procedure was tested by applying it for simple examples, for which the results are known. The numerical results were also compared with existing models for textile composites. In both cases, the results compare very favorably. The finite element procedure is extended to compute the thermal residual microstresses and to estimate the initial failure envelope for the textile composite.

An independent finite element micromechanical analysis, analogous to the above, is presented for thin textile composite structures with few unit-cells in the thickness direction. In that case, the composite is modeled as a homogeneous plate to predict the plate stiffness coefficients and plate coefficients of thermal expansion. It was shown the plate properties could not be predicted from the corresponding three-dimensional properties.

In addition, an approximate analytical procedure is presented to estimate the composite thermo-elastic constants. The procedure called the Selective Averaging Method is based on a judicious combination of stiffness and compliance averaging. The method is fast and easy to implement, and suitable for parametric studies.

CHAPTER 1
INTRODUCTION

1.1 Background

The increasing demand for lightweight yet strong and stiff structures has lead to the development of advanced fiber reinforced composites. These materials are not only used in the aerospace industry but also in a variety of commercial applications like automobile, marine and biomedical applications. Traditionally fibrous composites are manufactured by laminating several layers of unidirectional fiber tapes (Fig. 1) pre-impregnated with matrix material. The effective properties of the composite can be controlled by changing several parameters like the fiber orientation in a layer, stacking sequence, fiber and matrix material properties and fiber volume fraction. However, the manufacture of fibrous laminated composites from prepregs is labor intensive. Besides, laminated composites lack through-the-thickness reinforcement, and hence have poor interlaminar strength and fracture toughness.
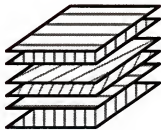
Figure 1.   Stacking of layers (plies) for fibrous laminated composite.

Figure 2.   Examples of woven, braided and knitted textile preforms. (Source: Chou and Ko, 1989)
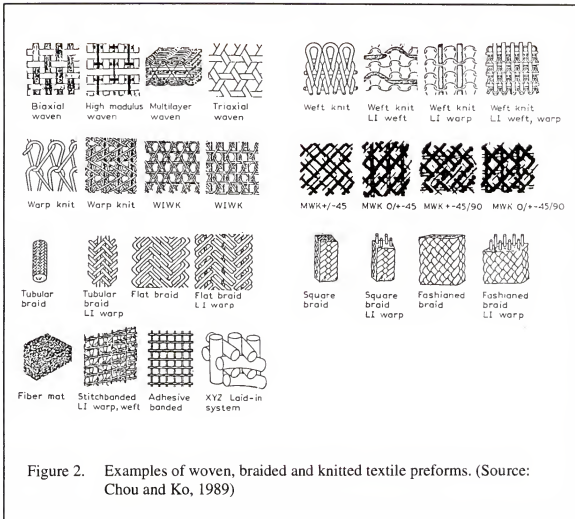
Recent developments in textile manufacturing processes show some promise in overcoming the above limitations. Textile processes such as weaving, braiding and knitting can turn large volumes of yarn into dry preforms at a faster rate, thus reducing costs and cycle time. The dry preforms (Fig. 2) are impregnated with appropriate matrix material and cured in a mold using processes such as Resin Transfer Molding (RTM). Two-dimensional woven and braided mats offer increased through the thickness properties due to yarn interlacing. The mats may be stitched using Kevlar or glass threads to provide additional reinforcement along the thickness direction (Sharma and Sankar, 1995). Three-dimensional woven and braided composites provide multidirectional reinforcement, thus directly enhancing the strength and stiffness in the thickness direction. Unlike laminated structures

three-dimensional composites do not possess the weak plane of delamination, thus giving increased impact resistance and fracture toughness. Textile manufacturing processes in conjunction with resin transfer molding are also suitable for the production of intricate structural forms at a reduced cycle time. This allows complex shaped structures to be fabricated as an integral unit, thus eliminating the use of joints and fasteners.

With the advancements in aforementioned technologies there is a need to develop scientific methods of predicting the performance of the composites made using the above processes. There are numerous variables involved in textile processes besides the choice of the fiber and matrix materials. This, for example, includes (a) the number of filaments in the yarn specified by the yarn linear density and (b) the yarn architecture (description of the yarn geometry) determined by the type of weaving or braiding processes. Thus, there is a need for analytical/numerical models to study the effect of these variables on the textile composite behavior.

Ideally a structural engineer would like to model textile composites as a homogeneous anisotropic material—preferably orthotropic—so that the structural computations can be simplified, and also the existing computer codes can be used in the design. This would require the prediction of the effective (macroscopic) properties of the composites from the constituent material (microscopic) characteristics such as yarn and matrix properties, yarn-matrix interface characteristics and the yarn architecture (Fig. 3). This is possible if we assume that there is a representative volume element (RVE) or an unit-cell that repeats its self throughout the volume of the composite, which is true in the case of textile composites. The unit-cell can be considered as the smallest possible building block for the textile composite, such that the composite can be created by assembling the unit-cell in all three dimensions (Fig. 4). The prediction of the effective macroscopic properties from the constituent material characteristics is one of the aspects of the science known as *micromechanics*. The effective properties include thermo-mechanical properties like

stiffness, strength and coefficients of thermal expansion as well as thermal conductivities, electromagnetic and other transport properties.

Figure 3.   Essence of micromechanics.
(a) composite (microscale) showing plain-weave pattern
(b) homogeneous and orthotropic composite (macroscale).

Figure 4.   Unit-cell for a textile composite.
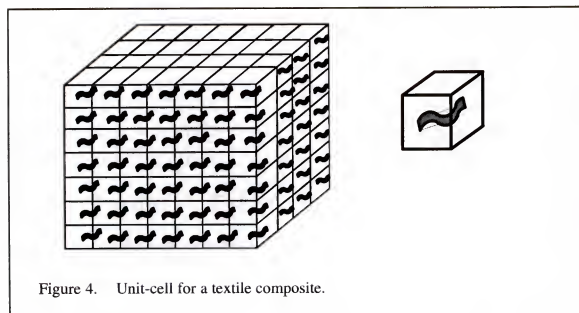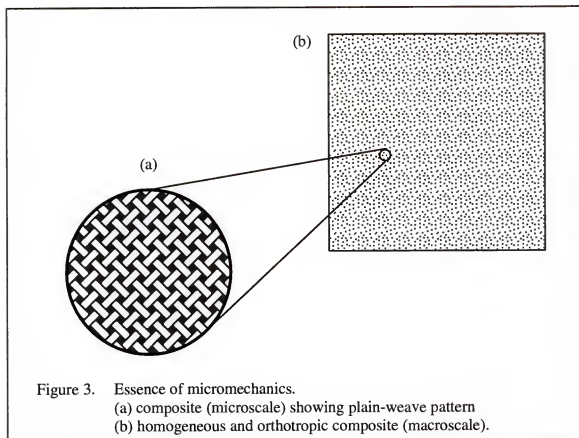
Most of the early work to determine the properties of heterogeneous materials was restricted to particulate (spherical) inclusions which were assumed to be isotropic. For example, Hashin (1962) derived expressions for the bounds for the elastic moduli of heterogeneous materials using variational theory. A review of analytical methods for predicting the effective properties of particulate composites was presented by Christensen (1990). However, the complex geometry of the textile preforms makes such precise analytical modeling difficult.

The current literature dealing with micromechanical analyses for textile composites can be broadly classified into three categories: mechanics of materials type models, energy based approach, and finite element analysis of the unit-cell. All of the above models recognize that there is a unit-cell in the composite material, and they attempt to model the material as a homogeneous orthotropic material. In the mechanics of materials type models, the yarns are approximated as simple structural elements, *e.g.*, beams, plates, laminates etc., and their deformation behavior is assumed to be governed by the corresponding structural constitutive relations. The kinematics is also simplified to a great extent, and a relation between the overall deformation of the unit-cell and the average forces are derived. The energy approach is similar to the previous one, except that the strain energy in the unit-cell is evaluated based on some assumed displacement field, which is usually an oversimplification of exact displacements. The elastic constants are derived by equating the strain energy in the approximate model to that in an idealized homogeneous composite. Most energy based approaches provide bounds for the homogeneous properties, and can be used as a check for experimental observations or other theoretical models. The third method is the rigorous micromechanical analysis of the unit-cell, which often requires the use of numerical methods such as the finite element method, and also uses the exact three-dimensional constitutive relations for the yarn and the matrix material.

Ishikawa and Chou (1982a, 1982b, 1983a, 1983b, 1983c) proposed three analytical models for thermo-elastic properties of woven fabric composites—the mosaic model, the

fiber undulation model and bridging model. The mosaic model treats the composite as an assembly of crossply laminates, and then uses lamination theory to predict the composite properties. The fiber undulation model in addition takes into account the effect of yarn continuity in the loading direction. The bridging model was specifically developed to estimate the elastic behavior of satin weaves. This model simulates the effect of load distribution and load transfer between the yarns. The above three models were developed for two-dimensional fabric composites. These models were then extended by Yang et al. (1986) in the fiber inclination model to predict the elastic properties of three-dimensional textile composites. The fiber inclination model was used to determine the elastic properties of three-dimensional angle-interlock composites and braided composites by Whitney and Chou (1989) and Ma et al. (1986) respectively. The results were compared with test data, and parametric analyses were performed to study the effect of changing geometric parameters. Crane and Camponeschi (1986) presented an analytical model based on classical lamination theory to predict the extensional stiffnesses for multi-directional braided composites. Naik (1994) used a stiffness averaging technique to predict woven and braided composite properties (explained in Chapter 3).

Numerical modeling of the unit-cell is popular due to its ability to capture the effects of complicated yarn architectures. For instance, Yoshino and Ohtsuka (1982) performed a two-dimensional finite element analysis using plane strain elements to predict the stress distribution within a plain-weave fabric. Dasgupta et al. (1990) and Whitcomb (1991) analyzed the unit-cell of a plain-weave composite using three-dimensional finite elements to determine the effect of the yarn geometry and yarn volume fraction on the composite thermo-elastic constants. Foye (1993) used inhomogeneous elements called replacement elements to model the unit-cell. His model can be used to predict both composite stiffness and strength properties. Cox et al. (1994) presented a three-dimensional finite element model using two types of elements. The yarns are modeled as two-node line elements and the rest of the medium as eight-node solid elements. The model was used to predict failure

mechanisms in angle and orthogonal interlock woven composites. Raju et al. (1990) compiled a review of available analytical and numerical methods for modeling textile composites.

1.2 Scope of Study

The analytical models explained above are approximate—they make use of assumptions similar to that in classical plate theory, and the yarn geometry is greatly simplified. Further, these models do not consider periodic boundary conditions (see Section 2.1.1) for continuity of displacements and tractions on opposite faces of the unit-cell. Most of the existing numerical models are for specific yarn geometries such as simple weave architectures. Therefore there is a need for more general models to predict the mechanical properties for a textile composite, particularly for composites with complex woven and braided geometries. The present study illustrates two such methods. The first method involves rigorous finite element analysis of the unit-cell, which imposes exact displacement and traction boundary conditions on the end-faces of the unit-cell. The second is an approximate analysis in which the unit-cell is discretized into a number of elements. The effective (macroscale) stiffness for the composite is computed by a combination of stiffness and compliance averaging of the element stiffness coefficients. The advantage of the proposed methods is their generality—they are applicable to any textile geometry provided that there exists a repeatable pattern (which defines the unit-cell). Both the methods can compute the effective elastic constants and effective coefficients of thermal expansion for the homogenous composite.

The analysis for the elastic constants of the textile composite continuum assumes that the unit-cell is repeatable in all three dimensions. This assumption will not be valid for thin textile composite structures, where there will be a only a few unit-cells in the thickness direction. For such applications, an alternate micromechanical analysis is proposed. The

unit-cell is modeled as a plate (Fig. 5) and the corresponding plate stiffness coefficients and plate coefficients of thermal expansion are predicted.
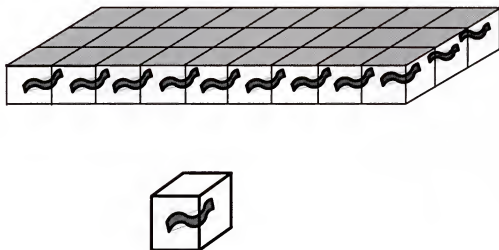
Figure 5. Textile composite plate showing unit-cell.

Chapter 2 explains the finite element procedure to compute the macroscale thermo-elastic constants. The procedure is detailed for a thick textile composite in which there are sufficient number of unit-cells in the thickness direction. The procedure is then extended to a thin composite. The thin composite is first modeled as a beam and a two-dimensional analysis is presented to compute the beam thermo-elastic coefficients. A similar three-dimensional analysis is also illustrated in which the thin composite is modeled as a plate. An analytical procedure called the Selective Averaging Method (SAM) is presented in Chapter 3 to estimate the macroscale thermo-elastic constants. This procedure utilizes a judicious combination of stiffness and compliance averaging to compute the composite properties. Again for a thin textile composite the plate stiffness coefficients and plate coefficients of thermal expansion may be computed.

In Chapter 4 the microstresses computed using the finite element analysis, are used to construct an initial failure envelope for a textile composite modeled as homogeneous continuum. An independent procedure using plate theory is presented to predict the failure envelope for a thin textile composite. Since the composite is generally fabricated at a temperature greater than room temperature, thermal residual microstresses are developed due to the mismatch in the coefficients of thermal expansion for the constituent materials. A method to predict these thermal microstresses is illustrated. Chapter 5 deals with the issues pertaining to finite element modeling of the unit-cell. Due to the complex yarn architectures, traditional finite element modeling becomes exceedingly difficult. Various alternative means of finite element modeling the unit-cell are discussed with suitable two-dimensional examples. Finally Chapter 6 summarizes the work done in this study. The limitations of the work are addressed and suggestions are given for future work in this area.

CHAPTER 2
FINITE ELEMENT MODELS FOR THERMO-ELASTIC CONSTANTS

In this chapter, we demonstrate finite element based micromechanical models to predict the effective stiffness properties and effective coefficients of thermal expansion (CTE's) for a textile composite. The macroscale properties of the composite are determined at a scale much larger than the dimensions of the unit-cell, but comparable to the dimensions of the structural component. The average stresses at a point at the structural scale will be called the macroscale stresses or macrostresses. The actual stresses at a point at the continuum level will be called the microscale stresses or microstresses. To distinguish the macroscale deformations and stresses from their microscale counterparts—a superscript "M" will be used to denote the macroscale deformations and stresses.

2.1 Unit-Cell Analysis for Three-Dimensional Elastic Constants

In this section a procedure to determine the three-dimensional elastic constants for a textile composite material is described. Consider a rectangular hexahedron as the unit-cell of the three-dimensional textile composite. The edges of the unit-cell are assumed to be parallel to the coordinate axes x_1, x_2 and x_3, with unit-cells repeating in all three directions. The length of the unit-cell in the x_i direction is defined as L_i. On the macroscale the composite is assumed to be homogeneous and orthotropic and the composite behavior is characterized by the following constitutive relation :

$$\begin{Bmatrix} \sigma_{11}^M \\ \sigma_{22}^M \\ \sigma_{33}^M \\ \tau_{23}^M \\ \tau_{31}^M \\ \tau_{12}^M \end{Bmatrix} = [C] \left\{ \begin{Bmatrix} \varepsilon_{11}^M \\ \varepsilon_{22}^M \\ \varepsilon_{33}^M \\ \gamma_{23}^M \\ \gamma_{31}^M \\ \gamma_{12}^M \end{Bmatrix} - \begin{Bmatrix} \alpha_1^c \\ \alpha_2^c \\ \alpha_3^c \\ \alpha_{23}^c \\ \alpha_{31}^c \\ \alpha_{12}^c \end{Bmatrix} \Delta T^M \right\} \tag{1}$$

where $\{\sigma^M\}$ and $\{\varepsilon^M\}$ are the macrostresses and macrostrains, respectively; $\{\alpha^c\}$ and $[C]$ are the macroscale CTE's and orthotropic elasticity matrix to be determined; ΔT^M is a uniform temperature difference throughout the unit-cell. The macroscale elasticity matrix is of the form:

$$[C] = \begin{bmatrix} C_{11} & C_{12} & C_{13} & C_{14} & C_{15} & C_{16} \\ & C_{22} & C_{23} & C_{24} & C_{25} & C_{26} \\ & & C_{33} & C_{34} & C_{35} & C_{36} \\ & symm. & & C_{44} & C_{45} & C_{46} \\ & & & & C_{55} & C_{56} \\ & & & & & C_{66} \end{bmatrix} \tag{2}$$

The unit-cell analysis assumes that the material is homogeneous and orthotropic on the macroscale. The material, therefore, is subject to a uniform state of strain in the macroscopic sense. The macrostresses required to create such a state of strain are computed from the finite element model of the unit-cell. In the microscale, all unit-cells have identical stress and strain fields. Continuity of microstresses across the unit-cell then requires that tractions be equal and opposite at corresponding points on opposite faces of the unit-cell. Since the displacement gradients are constant for a homogeneous deformation, the displacements at corresponding points on opposite faces of the unit-cell differ only by a constant.

2.1.1 Periodic Boundary Conditions

The periodic boundary conditions (BC's) consist of the periodic displacement boundary conditions which ensure the compatibility of displacements on opposite faces of the unit-cell, and the periodic traction boundary conditions to enforce the continuity of stresses. A macroscopically homogeneous deformation can be represented as

$$u_i^M \; = \; H_{ij}x_j \qquad i,j \; = \; 1,2,3 \tag{3}$$

where H_{ij} are the displacement gradients. Then the periodic displacement boundary conditions to be imposed on the faces $x_i=0$ and $x_i=L_i$ are

$$\begin{aligned}
u_i(L_1,x_2,x_3) - u_i(0,x_2,x_3) &= H_{i1}L_1 \\
u_i(x_1,L_2,x_3) - u_i(x_1,0,x_3) &= H_{i2}L_2 \\
u_i(x_1,x_2,L_3) - u_i(x_1,x_2,0) &= H_{i3}L_3
\end{aligned} \tag{4}$$

The traction boundary conditions to be imposed on the faces $x_i=0$ and $x_i=L_i$ are

$$\begin{aligned}
F_i(L_1,x_2,x_3) &= -F_i(0,x_2,x_3) \\
F_i(x_1,L_2,x_3) &= -F_i(x_1,0,x_3) \\
F_i(x_1,x_2,L_3) &= -F_i(x_1,x_2,0)
\end{aligned} \tag{5}$$

The periodic displacement and traction BC's (for a two-dimensional problem) to be imposed for the deformation given by $\varepsilon_{11}=1/L_1$ and $\varepsilon_{22}=\gamma_{12}=0$ are shown in Fig. 6.

The above periodic BC's are imposed in the finite element model either by using multi-point constraint elements or by incorporating transformation equations to eliminate the constrained displacements (Cook et al., 1989). These two methods to impose the periodic BC's are discussed in Section 5.1.3. Both the methods require a finite element model with corresponding nodes on opposite faces of the unit-cell.

$$u_1^m - u_1^n = 1 \qquad u_1^p - u_1^q = 0$$
$$u_2^m - u_2^n = 0 \qquad u_2^p - u_2^q = 0$$

$$F_1^m = -F_1^n \qquad F_1^p = -F_1^q$$
$$F_2^m = -F_2^n \qquad F_2^p = -F_2^q$$
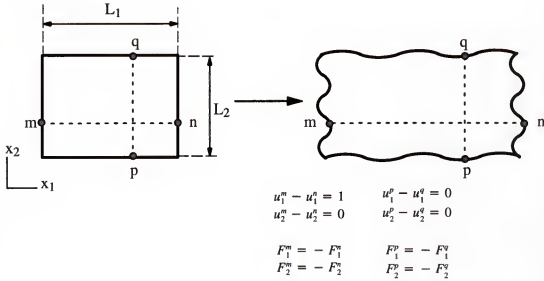
Figure 6. Two-dimensional example illustrating the periodic boundary conditions for the the deformation $\varepsilon_{11} = 1/L_1$ and $\varepsilon_{22} = \gamma_{12} = 0$.

2.1.2 Determination of Three-Dimensional Elastic Constants and CTE's

The unit-cell is discretized with three-dimensional finite elements such that opposite faces of the unit-cell have identical nodes. Periodic displacement and traction boundary conditions are enforced between the corresponding nodes. The periodic displacement BC's are imposed such that only one of the macrostrain components is non-zero; and the uniform temperature difference ΔT^M is set to zero. Then, the difference in displacements between corresponding points on opposite faces of the unit-cell will be equal to that in a homogenous continuum subject to the same deformation. The average stresses (macrostresses) required to create such a deformation are obtained from the finite element results. Substituting the macrostresses and macrostrains in the composite constitutive relation (Eqn. 1) the stiffness coefficients in the column corresponding to the non-zero strain can be evaluated. This procedure is repeated for other macrostrain components (keeping the temperature difference

zero) to obtain the entire stiffness matrix $[C]$. The orthotropic elastic constants of the composite material can be easily determined by inverting the stiffness matrix, and comparing the compliance coefficients with that of an orthotropic material.

To compute the six CTE's, a finite temperature change T_o is applied to all the elements in the unit-cell; and periodic displacement BC's are imposed such that all the macrostrain components are zero. Then the composite constitutive relation Eqn. (1) will reduce to

$$\{\sigma^M\} = -[C]\{\alpha^c\} \ T_o \tag{6}$$

The macrostresses for such a deformation are computed as described below. Knowing the stiffness matrix $[C]$, the composite CTE's are found as

$$\{\alpha^c\} = -\frac{1}{T_o}[C]^{-1}\{\sigma^M\} \tag{7}$$

Table 1 presents the non-zero displacement BC's imposed on the unit-cell to obtain $[C]$ and the CTE's $\{\alpha^c\}$.

Table 1.   Non-zero displacement BC's to obtain 3-D elastic constants and CTE's.

stiffness coefficients to be obtained	non-zero displacement BC's
first column of $[C]$ ($\varepsilon_{11}{}^M = 1$)	$u_1(L_1, x_2, x_3) - u_1(0, x_2, x_3) = L_1$
second column of $[C]$ ($\varepsilon_{22}{}^M = 1$)	$u_2(x_1, L_2, x_3) - u_2(x_1, 0, x_3) = L_2$
third column of $[C]$ ($\varepsilon_{33}{}^M = 1$)	$u_3(x_1, x_2, L_3) - u_3(x_1, x_2, 0) = L_3$
fourth column of $[C]$ ($\gamma_{23}{}^M = 1$)	$u_2(x_1, x_2, L_3) - u_2(x_1, x_2, 0) = L_3/2$
	$u_3(x_1, L_2, x_3) - u_3(x_1, 0, x_3) = L_2/2$
fifth column of $[C]$ ($\gamma_{13}{}^M = 1$)	$u_1(x_1, x_2, L_3) - u_1(x_1, x_2, 0) = L_3/2$
	$u_3(L_1, x_2, x_3) - u_3(0, x_2, x_3) = L_1/2$
sixth column of $[C]$ ($\gamma_{12}{}^M = 1$)	$u_1(x_1, L_2, x_3) - u_1(x_1, 0, x_3) = L_2/2$
	$u_2(L_1, x_2, x_3) - u_2(0, x_2, x_3) = L_1/2$
CTE's ($\Delta T^M = 1$)	$\Delta T = 1$

The macrostresses for a given deformation state can be found by the following two methods. In the first method, the macrostresses are obtained by averaging the nodal forces on each face of the unit cell. For example, the macroscale σ_{11}^M can be obtained as

$$\sigma_{11}^M = \frac{1}{L_2 L_3} \sum_n F_1^{(n)}(L_1, x_2, x_3) \tag{8}$$

where $F_1^{(n)}$ is the nodal force in the x_1 direction at the nth node, and $\sum_n$ denotes summation over all nodes on the face $x_1 = L_1$. Alternatively, the macrostresses can be computed by volume-averaging the corresponding microstress component in the unit-cell. Then the macrostress component σ_{11}^M is obtained as

$$\sigma_{11}^M = \frac{1}{V} \int_V \sigma_{11}(x, y, z) dV \tag{9}$$

where V is the volume of the unit-cell. The microstresses are computed at the quadrature points, and numerically integrated over the volume in each element of the unit-cell.

2.1.3 Results and Discussion for 3-D Elastic Constants and CTE's

The above procedure was demonstrated for the following material systems:

Example 1.   isotropic material

Example 2.   bimaterial medium—both materials are assumed isotropic (Fig. 7)

Example 3.   unidirectional composite with identical Poisson ratios for fiber and matrix— fiber and matrix materials are isotropic (Fig. 8)

Example 4.   unidirectional composite with different Poisson ratios for fiber and matrix— fiber and matrix materials are isotropic

Example 5.   plain-weave textile composite (Fig. 9)—yarn geometry and properties obtained from Dasgupta et al. (1990)

Example 6.   plain-weave textile composite—yarn geometry and properties obtained from Naik (1994)

Example 7.   5-harness satin weave (Fig. 10)—yarn geometry and properties obtained

        from Naik (1994)

For the textile composite examples (examples 5-7), the yarn is assumed to be transversely

isotropic and the matrix material is assumed isotropic. The constituent material properties

for the examples are listed in Table 2.

Table 2.   Properties of constituent materials for examples 1–7.

Example 1		$E = 10\ GPa,\ \nu=0.3,\ \alpha=10x10^{-6}/^oC$
	unit-cell size:	$0.500x0.500x0.256\ mm$
Example 2	layer 1 (E–glass):	$E_1=70\ GPa,\ \nu_1=0.200,\ \alpha_1=5x10^{-6}/^oC,\ V_1=0.5$
	layer 2 (epoxy):	$E_2=3.50\ GPa,\ \nu_2=0.350,\ \alpha_2=60x10^{-6}/^oC,\ V_2=0.5$
	unit-cell size:	$0.500x0.500x0.256\ mm$
Example 3	fiber:	$E_f=100\ GPa,\ \nu_f=0.300,\ \alpha_f=10x10^{-6}/^oC,\ V_f=0.6$
	matrix:	$E_m=10\ GPa,\ \nu_m=0.300,\ \alpha_m=100x10^{-6}/^oC$
	unit-cell size:	$10x10x10\ \mu m$
Example 4	fiber (E–glass):	$E_f=70\ GPa,\ \nu_f=0.200,\ \alpha_f=5x10^{-6}/^oC,\ V_f=0.6$
	matrix (epoxy):	$E_m=3.50\ GPa,\ \nu_m=0.350,\ \alpha_m=60x10^{-6}/^oC$
	unit-cell size:	$10x10x10\ \mu m$
Example 5	yarn (glass-epoxy):	
	$E_L=58.61\ GPa,\ E_T=14.49\ GPa,\ G_{LT}=5.38\ GPa,\ \nu_{LT}=0.250$	
	$\nu_{TT}=0.247,\ \alpha_L=6.15x10^{-6}/^oC,\ \alpha_T=22.64x10^{-6}/^oC,\ V_f=0.26$	
	matrix (epoxy):	
	$E=3.45\ GPa,\ \nu=0.37,\ \alpha=69x10^{-6}/^oC$	
	unit-cell size:	$1.680x1.680x0.228\ mm$
Examples 6, 7	yarn (graphite-epoxy):	
	$E_L=144.80\ GPa,\ E_T=11.73\ GPa,\ G_{LT}=5.52\ GPa,\ \nu_{LT}=0.230$	
	$\nu_{TT}=0.300,\ \alpha_L=-0.324x10^{-6}/^oC,\ \alpha_T=14.00x10^{-6}/^oC,\ V_f=0.64$	
	matrix (epoxy):	
	$E=3.45\ GPa,\ \nu=0.35,\ \alpha=40x10^{-6}/^oC$	
	unit-cell size:	$2.822x2.822x0.2557\ mm\ (Example\ 6)$
		$7.055x7.055x0.2557\ mm\ (Example\ 7)$

V_i *stands for the volume fraction of the constituent material*
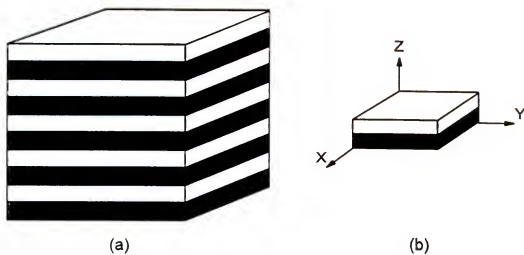
Figure 7. Bimaterial example.
(a) bimaterial medium; (b) unit-cell.
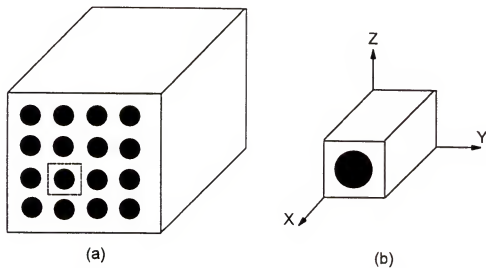
Figure 8. Unidirectional composite example.
(a) composite; (b) unit-cell.
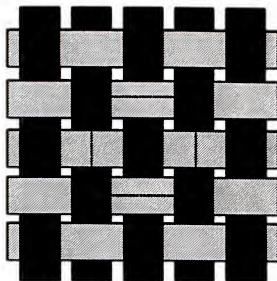
Figure 9.   Yarn pattern in a plain weave preform. (unit-cell boundary in dotted lines)
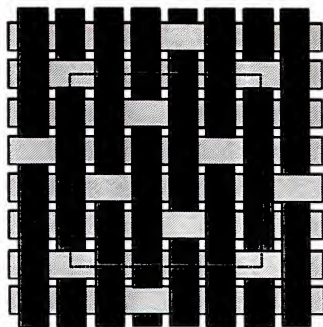
Figure 10.   Yarn pattern in a 5-harness satin weave preform. (unit-cell boundary in dotted lines)

A 3-D finite element code called $\mu TE\chi$–10 (pronounced as *microtech*) was written and implemented for the seven examples to compute the homogeneous elastic constants and CTE's. The unit-cell was assumed to be a rectangular hexahedron with edges along the x-, y- and z- axes. The unit-cell was divided into uniform-sized eight-node brick elements as shown in Figure 11. The number of divisions along the x-, y- and z- axes are specified by the user. The elements were in general, inhomogeneous elements, *i.e.*, consisted of more than one constituent material. While computing the element stiffness matrix, the material property at the Gauss integration points was determined, and the corresponding elasticity matrix was used to perform the integration over the element volume (see Section 5.1.2). Thus the element stiffness matrix was obtained as the averaged stiffness of the different materials in the element. Periodic displacement and traction boundary conditions were imposed between corresponding nodes on opposite faces of the unit-cell. The numerical procedure to compute the element stiffness matrix and to impose periodic BC's are discussed in Chapter 5. The skyline solver (Bathe, 1982) was used to solve for the nodal displacements. The computed elastic constants for the seven examples are listed in Tables 3-5.

Figure 11. 3-D finite element mesh to compute elastic constants.
(a) unit-cell; (b) eight-node brick element.
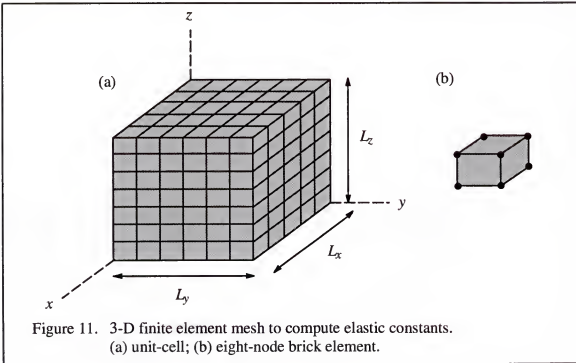
The $\mu TE\chi$–10 code was first checked by computing the elastic constants for an isotropic medium (Table 3). Then the code was implemented for a bimaterial medium. The bimaterial medium consisted of two different layers of equal thickness in the xy-plane alternating in the z-direction (Fig. 7). The effective Young's moduli, Poisson ratios and CTE's of the bimaterial medium were derived exactly, as described below. The constitutive relation (considering only the normal stresses) for each layer is defined as:

$$\begin{Bmatrix} \sigma_{xx}^i \\ \sigma_{yy}^i \\ \sigma_{zz}^i \end{Bmatrix} = \begin{bmatrix} C_{11}^i & C_{12}^i & C_{13}^i \\ C_{12}^i & C_{22}^i & C_{23}^i \\ C_{13}^i & C_{23}^i & C_{33}^i \end{bmatrix} \begin{Bmatrix} \varepsilon_{xx}^i \\ \varepsilon_{yy}^i \\ \varepsilon_{zz}^i \end{Bmatrix} \qquad i = 1, 2 \qquad (10)$$

where the superscript refers to the layer number. To derive C_{11}, C_{12} and C_{13} for the bimaterial medium, ε_{xx}^M was assumed as one; and ε_{yy}^M and ε_{zz}^M were assumed to be zero. The assumption of $\varepsilon_{zz}^M = 0$ and the fact that the layers are of equal thickness imply that $\varepsilon_{zz}^1 = -\varepsilon_{zz}^2$. The following constraints were, in addition, imposed across the bimaterial interface :

$$\begin{aligned} \varepsilon_{xx}^1 &= \varepsilon_{xx}^2 = \varepsilon_{xx}^M \\ \varepsilon_{yy}^1 &= \varepsilon_{yy}^2 = \varepsilon_{yy}^M \\ \sigma_{zz}^1 &= \sigma_{zz}^2 = \sigma_{zz}^M \end{aligned} \qquad (11)$$

From the above interfacial constraints and Eqn. (10), the stresses in each layer were computed. The stresses in the layers were volume-averaged to yield the corresponding macrostresses, i.e., σ_{xx}^M, σ_{yy}^M and σ_{zz}^M. Since ε_{xx}^M was equal to unity, the computed macrostresses were identical to the stiffness coefficients in the first column, namely, C_{11}, C_{12} and C_{13}. A similar procedure was followed to find the remaining stiffness coefficients and CTE's for the bimaterial medium. The inplane shear modulus of the bimaterial medium was computed as $G_{xy} = (G_1 + G_2)/2$ knowing that the shear strain was uniform in both layers. The isostress assumption was used to derive the transverse shear modulus as $G_{xz} = \dfrac{2G_1 G_2}{G_1 + G_2}$.

It was found that $\mu TE\chi$–10 results were identical to the elasticity results for the bimaterial medium (Table 3).

Table 3.   Continuum properties for examples 1 and 2 using finite elements.

		E_x, E_y (GPa)	E_z (GPa)	G_{xz}, G_{yz} (GPa)	G_{xy} (GPa)	ν_{xz}, ν_{yz}	ν_{xy}	$\alpha_x{}^c, \alpha_y{}^c$ x 10^{-6}/°C	$\alpha_z{}^c$ x 10^{-6}/°C
Example 1 (isotropic medium)	$\mu TE\chi$–10 (FEA)	10	10	3.85	3.85	0.300	0.300	10	10
	exact solution	10	10	3.85	3.85	0.300	0.300	10	10
Example 2 (bimaterial medium)	$\mu TE\chi$–10 (FEA)	36.79	9.79	2.48	15.23	0.312	0.208	8.19	59.60
	exact solution	36.79	9.79	2.48	15.23	0.312	0.208	8.19	59.60

Table 4.   Continuum properties for examples 3 and 4 using finite elements.

		E_L (GPa)	E_T (GPa)	G_{LT} (GPa)	G_{TT} (GPa)	ν_{LT}	ν_{TT}	α_L x10^{-6} /°C	α_T x10^{-6} /°C
Example 3 (uni directional composite)	$\mu TE\chi$–10 (FEA)	63.55	36.48	12.93	9.94	0.300	0.232	15.74	40.79
	rule of mixt./ Halpin– Tsai eqns.	64	34.55	11.26	13.29	0.300	0.300	15.63	55.11
Example 4 (uni directional composite)	$\mu TE\chi$–10 (FEA)	43.12	18.15	5.59	3.92	0.242	0.222	7.40	25.44
	rule of mixt./ Halpin– Tsai eqns.	43.40	14.79	4.45	5.91	0.260	0.252	6.77	34.24

Table 4 presents the elastic constants and CTE's for the two unidirectional composite examples. The unidirectional composite unit-cell is shown in Fig. 8. The unidirectional

composite properties were compared with available analytical solutions. The rule of mixtures formulae were used to predict E_L and ν_{LT} ; the Halpin-Tsai equations (Halpin and Tsai, 1969) for E_T, G_{LT} and ν_{TT} and Schapery's expressions (Agarwal and Broutman, 1990) for the thermal coefficients a_L and a_T. To compare G_{TT}, transverse isotropy was assumed in the T-T plane and computed as $\dfrac{E_T}{2(1+\nu_{TT})}$. However, the finite element results show that the assumption of isotropy in the transverse plane is not valid. The assumption would give G_{TT} as 14.81 GPa and 7.43 GPa for examples 3 and 4 respectively, thus grossly over-estimating the finite element results. The relations for E_L, ν_{LT} and a_L are exact when the poisson ratios are identical for the fiber and the matrix.

Table 5.   Continuum properties for examples 5, 6 and 7 using finite elements.

		E_x, E_y (GPa)	E_z (GPa)	G_{xz}, G_{yz} (GPa)	G_{xy} (GPa)	ν_{xz}, ν_{yz}	ν_{xy}	$a_x{}^c, a_y{}^c$ x10^{-6}/ºC	$a_z{}^c$ x 10^{-6}/ºC
Example 5 (plain-weave)	$\mu TE\chi$–10 (FEA)	11.81	6.14	1.84	2.15	0.408	0.181	28.36	79.57
	Dasgupta results	14.38	6.25	1.94	3.94	0.463	0.167	22.50	86.00
Example 6 (plain-weave)	$\mu TE\chi$–10 (FEA)	53.61	10.88	4.41	4.72	0.365	0.128	1.56	22.71
	TEXCAD	64.38	11.49	5.64	4.87	0.396	0.027	1.33	20.71
Example 7 (5-harness weave)	$\mu TE\chi$–10 (FEA)	64.51	11.33	4.45	4.85	0.329	0.047	1.55	22.03
	TEXCAD	66.33	11.51	4.93	4.89	0.342	0.034	1.46	21.24

Figures 9 and 10 illustrate the weave patterns for the plain-weave (examples 5 and 6) and the 5-harness satin weave (example 7) respectively. The properties for example 5 were compared with Dasgupta's results for an overall fiber volume fraction (V_f) of 0.26. The yarn properties were not specified in Dasgupta et al. (1990). So the rule of mixtures and

Schapery's expressions were used to obtain the yarn properties from the given fiber and matrix properties. The $\mu TE\chi$–10 results for examples 6 and 7 were compared with TEXCAD —an approximate analytical method developed by Naik (1994). In both the examples the overall fiber volume fraction was 0.64. The unit-cell was divided into 13x13x7 elements for all three examples. The elastic constants for the three textile composite examples are presented in Table 5. It must be noted that $\mu TE\chi$–10 will marginally under-predict the stiffness moduli—since the yarn cross-section in the numerical model is approximated as a polygon inscribed within the actual cross-sectional area. Consequently the yarn/fiber volume fraction in the numerical model will always be less than the theoretical volume fraction.

2.2 Stress Gradient Effects

The methods explained in Section 2.1 assume that the unit-cells exist in all the three directions. This will be true in the case of thick textile composites. However there are many applications in which thin composites are used. In fact in order to take advantage of the properties of composites, the structures have to be made of thin plate like members with stiffeners for load transfer. In such cases there will be fewer unit-cells in the thickness direction. Thus the free surface effects will be predominant. There will be severe stress gradients through the thickness, and they will have an influence on the apparent stiffness and strength of the structure (Marrey and Sankar, 1993a; Sankar and Marrey; 1993a).

The following simple example will illustrate the stress gradient effects on stiffness. Consider a layered medium consisting of alternating layers of materials of equal thickness with Young's moduli E_1 and E_2 respectively (Fig. 12a). Any micromechanical model would predict that the medium can be considered as a homogeneous orthotropic material at macroscale and also the effective Young's modulus in the longitudinal direction is $(E_1+E_2)/2$, and there would not be any bending-stretching coupling in the principal material direction. However, if we consider a bimaterial beam consisting of the same two materials

(Fig. 12b), we will find that there is a bending-stretching coupling, and also the flexural rigidity cannot be predicted from the Young's modulus of the homogeneous orthotropic medium and the total beam thickness. The bimaterial beam has properties and behavior different from the corresponding infinite medium. This phenomenon is observed in the transverse shear behavior also (Sankar and Marrey, 1993b). A similar behavior is also expected in thin textile composites where there are fewer unit-cells in the thickness directions, and the unit-cells are not subjected to a macroscopically homogeneous state of deformation as assumed in Section 2.1.

(a)

(b)
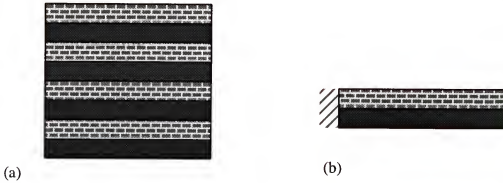
Figure 12.   Example to explain stress gradient effects.
(a) Layered medium; (b) Bimaterial beam.

One method of overcoming the above difficulties in thin textile composites is to model the composite as a plate/beam, and compute the structural stiffness properties (e.g., $[A]$, $[B]$ and $[D]$ of the plate) directly from the unit-cell analysis instead of the continuum stiffness properties such as Young's modulus, shear modulus etc. In the following sections we illustrate these concepts—first for a thin textile composite modeled as a beam (Sankar and Marrey, 1993b; Marrey and Sankar, 1993b) and then for a textile composite plate. The purpose of the beam model is to present the issues involved in computing the structural

stiffness coefficients as opposed to continuum elastic constants. Further the periodic BC's are different from those in the continuum model.

2.3 Unit-Cell Analysis for Beam Thermo-Mechanical Coefficients

In this section, a procedure for finding the equivalent flexural stiffness properties and thermal coefficients of a textile structural composite beam is described. The textile composite beam is assumed to be in the xz-plane with unit-cells repeating in the x-direction. A state of plane strain parallel to the xz-plane is assumed. On the macroscale it is assumed that the beam is homogeneous and its behavior can be characterized by the following beam constitutive relation :

$$\begin{Bmatrix} P \\ M \\ V \end{Bmatrix} = \begin{bmatrix} K_{11} & K_{12} & K_{13} \\ K_{12} & K_{22} & K_{23} \\ K_{13} & K_{23} & K_{33} \end{bmatrix} \left\{ \begin{Bmatrix} \varepsilon_o^M \\ \varkappa^M \\ \gamma_o^M \end{Bmatrix} - \begin{Bmatrix} \alpha_P \\ \alpha_M \\ \alpha_V \end{Bmatrix} \Delta T^M \right\} \tag{12}$$

where P, M and V are the axial force, bending moment and transverse shear force resultants, respectively; $[K]$ is the symmetric matrix of beam stiffness coefficients; ε_o^M, $\varkappa^M$ and γ_o^M are the midplane axial strain, curvature and transverse shear strain respectively; α_P, α_M and α_V, respectively, are the beam thermal expansion, thermal bending and thermal shear coefficients. The midplane deformations are related to the midplane axial displacement u_o, transverse displacement w, and rotation ψ as:

$$\varepsilon_o^M = \frac{\partial u_o^M}{\partial x}, \quad \varkappa^M = \frac{\partial \psi^M}{\partial x}, \quad \gamma_o^M = \psi^M + \frac{\partial w^M}{\partial x} \tag{13}$$

Actually, K_{11}, K_{12}, K_{22} and K_{33} are similar to the laminate stiffness coefficients A_{11}, B_{11}, D_{11} and $\varkappa^2 A_{55}$, respectively. There is no equivalence for K_{13} and K_{23} in the laminate theory, because the layers are assumed to be orthotropic, and they are rotated about the z-axis only. However, such a coupling between inplane deformations and transverse shear deformation may exist in textile composites as the fibers are inclined to the xy-plane unlike in the

laminates. The beam constitutive relation in Eqn. (12) can also be expressed in terms of compliance coefficients as:

$$\begin{Bmatrix} \varepsilon_o^M \\ \varkappa^M \\ \gamma_o^M \end{Bmatrix} = \begin{bmatrix} S_{11} & S_{12} & S_{13} \\ S_{12} & S_{22} & S_{23} \\ S_{13} & S_{23} & S_{33} \end{bmatrix} \begin{Bmatrix} P \\ M \\ V \end{Bmatrix} + \begin{Bmatrix} a_P \\ a_M \\ a_V \end{Bmatrix} \Delta T \qquad (14)$$

2.3.1 Beam Steady State Loading Conditions

Figure 13.   Steady state loading for a beam.
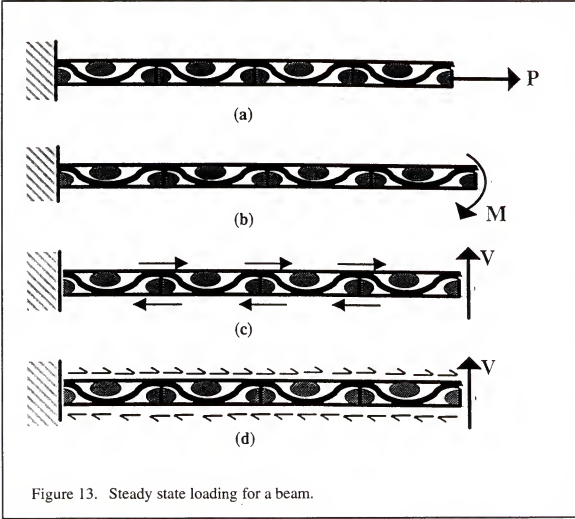
The continuum unit-cell analysis assumes that all the unit-cells are subjected to identical stress and strain fields, for a given state of loading. This is true in the case of constant axial force (P) and constant bending moment (M) in the beam (Figs. 13a and 13b).

However, when a shear force (V) is applied to the beam, the shear force will give rise to building up of bending moment at every cross-section, such that $V = -(dM/dx)$. This bending moment varies linearly over the length of the beam violating the assumption of homogeneous deformation. A state where the unit-cells are subjected to identical deformation under a shear force can be created by adding a couple periodically (Fig. 13c), or by having shear tractions on the top and bottom surfaces to cancel the bending moment continuously (Fig. 13d). In both cases traction-free conditions are violated on the top and bottom surfaces of the beam. As will be seen later, this situation creates difficulties in estimating the shear stiffness of the beam accurately.

2.3.2 Unit-Cell Boundary Conditions

The left end of the unit cell, $x=0$ (Fig. 14) are subject to minimum support constraints to prevent rigid body translation and rotation. The top and bottom surfaces of the beam are assumed to be traction free. The edges $x=0$ and $x=L$ have identical nodes in the finite element model and periodic BC's are enforced between these nodes. Three linearly independent deformations were applied to the unit-cell, in order to find the beam stiffness matrix $[K]$ namely,

Case (i)   unit axial strain ($\varepsilon_o^M = 1, \varkappa^M = 0, \gamma_o^M = 0$)

Case (ii)   unit curvature accompanied by transverse deflection such that the transverse shear strain was zero ($\varepsilon_o^M = 0, \varkappa^M = 1, \gamma_o^M = 0$)

Case (iii)   unit transverse shear strain ($\varepsilon_o^M = 0, \varkappa^M = 0, \gamma_o^M = 1$)

The periodic displacement constraints applied for each deformation case are presented in Table 6.

Table 6.   Periodic displacement BC's for beam unit-cell.

	$u(L,z)-u(0,z)$	$w(L,z)-w(0,z)$	ΔT
Case i. unit axial strain ($\varepsilon_0{}^M=1$)	L	0	0
Case ii. unit curvature ($\varkappa^M=1$)	Lz	$-L^2/2$	0
Case iii. unit shear strain ($\gamma_0{}^M=1$)	0	L	0

Consider the second deformation case, where a curvature is applied to the unit-cell. Let 'm' and 'n' be a set of corresponding nodes on the left and right ends of the unit-cell. The periodic BC's imposed between the nodes 'm' and 'n' are shown in Fig. 14. Applying a curvature to the unit-cell also induces transverse shear strain due to the ψ^M term in the expression for γ_0^M (Eqn. 13). The difference in displacement in the z-direction is therefore imposed to make the macroscopic transverse shear strain equal to zero.
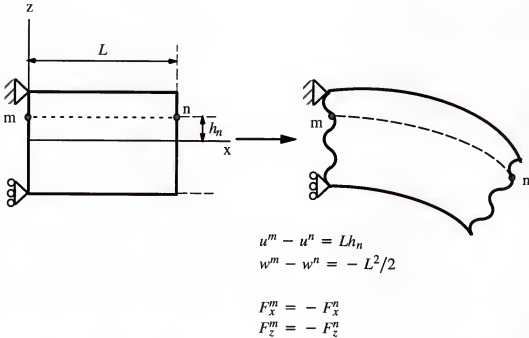

$$u^m - u^n = Lh_n$$
$$w^m - w^n = -L^2/2$$

$$F_x^m = -F_x^n$$
$$F_z^m = -F_z^n$$

Figure 14.   Boundary conditions pertaining to the deformation to $\varkappa^M \neq 0$, $\varepsilon_o{}^M=0$, $\gamma_o{}^M=0$.

2.3.3 Determination of Beam Stiffness Coefficients

The three linearly independent deformations described in the preceding section are applied to the unit-cell. The temperature difference (ΔT) is set to zero for all three deformations. For each case, the axial force P, the bending moment M_c and the shear force resultant V are computed from the nodal forces at the ends of the unit-cell. As explained earlier, the axial force and shear force are constant through the unit-cell, but the bending moment varies linearly across the unit-cell length. Therefore the bending moment at the center of the unit-cell is used as the reference moment, which is obtained by averaging the bending moment resultants at the ends of the unit-cell. From the force resultants, a pseudo-stiffness matrix $[k]$ can be computed that relates the forces and deformations as

$$\begin{bmatrix} k_{11} & k_{12} & k_{13} \\ k_{21} & k_{22} & k_{23} \\ k_{31} & k_{32} & k_{33} \end{bmatrix} \begin{Bmatrix} \varepsilon_o^M \\ \varkappa^M \\ \gamma_o^M \end{Bmatrix} = \begin{Bmatrix} P \\ M_c \\ V \end{Bmatrix} \tag{15}$$

For example, k_{11}, k_{21} and k_{31} will correspond to the values of P, M_c and V obtained for the case of unit axial extension of the unit-cell (Case i). The pseudo stiffness matrix, in general will not be symmetric since it does not relate corresponding forces and deformations (conjugate quantities, product of which yields an energy term)—it can be rather considered as a matrix of influence coefficients. The inverse of $[k]$, denoted by $[s]$ has some significance. The matrix $[s]$ is defined as

$$\begin{bmatrix} s_{11} & s_{12} & s_{13} \\ s_{21} & s_{22} & s_{23} \\ s_{31} & s_{32} & s_{33} \end{bmatrix} \begin{Bmatrix} P \\ M_c \\ V \end{Bmatrix} = \begin{Bmatrix} \varepsilon_o^M \\ \varkappa^M \\ \gamma_o^M \end{Bmatrix} \tag{16}$$

We know that $V=0$ is a steady state loading condition such that $M_c=M$, where M is the constant bending moment along the unit-cell. Noting that only the last column of $[s]$ multiplies with V, and comparing Eqns. (14) and (16), we can conclude that the first two columns of $[S]$ and $[s]$ must be identical to each other. Since $[S]$ is symmetric ($S_{13}=S_{31}$,

$S_{23}=S_{32}$), we can determine all but S_{33} of the beam compliance matrix $[S]$. An alternative approach to predict the shear compliance S_{33} is explained in the next section.

2.3.4 Determination of Beam Shear Stiffness

The difficulty in estimating S_{33} (or K_{33}) is associated with the inability to create a state of deformation such that only V is present. The shear modulus of the textile composite G_{xz} can be computed by assuming that the unit-cells span the material in the z-direction also. In that case periodic BC's are imposed between the top and bottom surfaces of the unit-cell, and the unit-cell is deformed transversely. Then, there will be shear tractions on the top and bottom surfaces of the beam—in fact this situation would correspond to Fig. 13(d). One may surmise that a shear correction factor $\varkappa^2$ could be found such that $K_{33}=\varkappa^2 G_{xz}h$. But a simple bimaterial beam example will show that the shear stiffness can be grossly underestimated.

Consider a bimaterial beam with layers of equal thickness ($h/2$). By performing a continuum unit-cell analysis the shear modulus of the material is found to be equal to $2G_1G_2 /(G_1+G_2)$. Assuming $G_1/G_2=10$, $G_{xz}=0.182\,G_1$. However the actual shear stiffness K_{33} is equal to $\varkappa^2(G_1+G_2)\,h/2$, which means that the apparent shear stiffness $G_{xz}=(G_1+G_2)/2 =0.55G_1$. This is about three times the previous estimate. This discrepancy is due to differing assumptions regarding the constancy of shear stress or shear strain. The continuum unit-cell analysis imposes constant shear stress in the two materials, and hence the shear compliance of the composite is the average of the compliances of the constituent materials. This is true when there are a large number of unit-cells in the z-direction. In a bimaterial beam, however, the shear strain is almost constant in the two layers, and hence the shear stiffness is the average of the shear stiffness of the individual layers—which is consistent with the method of computing A_{55} in the lamination theory. This illustrates the need for special procedures for predicting the shear stiffness of thin textile composite beams.

To overcome this problem we use an energy approach to compute the shear stiffness of a thin textile composite. We model a beam of length $2L$ consisting of two unit-cells, with

plane strain finite elements. The beam is subject to boundary conditions corresponding to pure shear strain (third boundary condition in Table 6). The top and bottom surfaces of the beam are traction free. The shear strain energy over a length L in the middle of the beam, U_s, is computed from the finite element results as

$$U_s = \sum_i \left(\frac{1}{2}\right) \tau^{(i)}_{xz} \gamma^{(i)}_{xz} A_i \qquad (17)$$

where $\tau^{(i)}_{xz}$ and $\gamma^{(i)}_{xz}$ are the shear stress and shear strain at the center of the ith element and A_i is the area of the ith element. The summation is performed over all elements located in a length L in the middle of the beam. Next, the shear strain energy over the same length L is computed using the beam formula:

$$U_s = \left(\frac{1}{2}\right) V \gamma_0 L = \left(\frac{1}{2}\right) V (S_{13}P + S_{23}M_c + S_{33}V) L \qquad (18)$$

In the above equation P, M_c and V can be obtained from the finite element results. The coefficients S_{13} and S_{23} have already been estimated. Then by equating the shear strain energy quantities in Eqns. (17) and (18), the only unknown, that is S_{33}, can be evaluated. The choice of two unit-cells to perform the above analysis deserves an explanation. When this was tried with one unit-cell for the cases of isotropic and bimaterial beam, the results were not good. It was mentioned earlier, that the application of a shear force would result in a couple at the unit-cell ends to continuously cancel the effect of the bending moment created along the beam length. This couple is manifested in the finite element results as concentrated forces at the four corners of the unit-cell, thus creating severe stress concentrations. When two unit-cells are used in the model, the stress concentrations remain in the corners of the beam, but their effects diminish in the middle portion of the beam. As will be seen in the later, the two unit-cell method gave very good K_{33} for both isotropic and bimaterial beams.

2.3.5 Determination of Beam CTE's

The procedure for determining the beam thermal expansion coefficients (Marrey and Sankar, 1993b) is as follows. The beam unit-cell is subject to a uniform temperature

difference given by $\Delta T = T_0$. The deformations in the beam are restrained by setting $\varepsilon_0{}^M = \varkappa^M = \gamma_0{}^M = 0$. Then the beam constitutive relation, Eqn. (12), will reduce to

$$\begin{Bmatrix} P \\ M_c \\ V \end{Bmatrix} = - \begin{bmatrix} K_{11} & K_{12} & K_{13} \\ K_{12} & K_{22} & K_{23} \\ K_{13} & K_{23} & K_{33} \end{bmatrix} \begin{Bmatrix} a_P \\ a_M \\ a_V \end{Bmatrix} T_0 \qquad (19)$$

The axial force P, the bending moment resultant at the center of the unit cell M_c and the shear force V are computed from the nodal forces at the ends of the unit-cell. Then the beam CTE's can be estimated from the expression,

$$\begin{Bmatrix} a_P \\ a_M \\ a_V \end{Bmatrix} = - \frac{1}{T_0} [K]^{-1} \begin{Bmatrix} P \\ M_c \\ V \end{Bmatrix} \qquad (20)$$

2.3.6 Results and Discussion

The procedures described above were implemented for the following cases:

(a)   an isotropic beam

(b)   a bimaterial beam with isotropic layers of equal thickness

(c)   a plain weave textile composite beam where the yarn is assumed to be transversely isotropic and the matrix is isotropic.

Table 7.   Constituent material properties for beam examples.

isotropic beam	$E = 10$ GPa, $\nu = 0.30$, $a = 10 \times 10^{-6}$ /ºC
bimaterial beam	$E_1 = 70$ GPa, $\nu_1 = 0.33$, $a_1 = 23 \times 10^{-6}$ /ºC $E_2 = 3.5$ GPa, $\nu_2 = 0.35$, $a_2 = 60 \times 10^{-6}$ /ºC
plain-weave textile beam	yarn: $E_1 = 159$ GPa, $E_2 = 10.9$ GPa, $G_{12} = 6.4$ GPa, $\nu_{12} = 0.38, \nu_{23} = 0.38$, $a_1 = 0.045 \times 10^{-6}$ /ºC, $a_2 = 20.2 \times 10^{-6}$ /ºC where the yarn direction is parallel to the 1–axis and the 23–plane is the plane of isotropy. matrix: $E_m = 3.5$ GPa, $\nu_m = 0.35$, $a_m = 60 \times 10^{-6}$ /ºC.

The properties of the constituent materials for all the cases are listed in Table 7. The dimensions of the unit-cell and the yarn architecture for the textile beam were taken from Yoshino and Ohtsuka (1982). The same unit-cell dimensions (length of 3.6 mm and height 1.8 mm) were also used for the isotropic and bimaterial cases. The unit-cell of the beam was discretized using eight-node isoparametric plane strain finite elements. The finite element mesh for the isotropic unit-cell and the plain weave unit-cell were identical except that different material properties were used.

Table 8.   Comparison of beam stiffness coefficients and CTE's (SI units).

		K_{11}	K_{12}	K_{22}	K_{33}	α_P /°C	α_M /°C
isotropic beam	unit-cell analysis	19.78×10^6	0	5.35	5.96×10^6	10×10^{-6}	0
	beam theory	19.78×10^6	0	5.34	5.77×10^6	10×10^{-6}	0
bimaterial beam	unit-cell analysis	74.29×10^6	30.20×10^3	20.06	8.47×10^6	30.73×10^{-6}	-14.62×10^{-3}
	beam theory	74.29×10^6	30.20×10^3	20.06	8.62×10^6	30.74×10^{-6}	-14.63×10^{-3}
textile beam	unit-cell analysis	27.76×10^6	0	5.41	9.21×10^6	12.66×10^{-6}	-24.12×10^{-6}
	mosaic model	71.48×10^{-6}	0	8.13	8.14×10^6	4.39×10^{-6}	0

Note: K_{13}, K_{23} and α_V are zero for all cases

The deformed unit-cells under various independent loading conditions are shown in Figs. 15 to 17. The stiffness and thermal coefficients for the three beams are shown in Table 8. The results for the isotropic and bimaterial beams were compared to exact beam theory solutions. Exact shear correction factors—0.833 for the isotropic beam and 0.555 for bimaterial beam (Whitney, 1973) were used in the beam theory solution to compute the shear stiffness given in Table 8. It can be seen from Table 8 that the beam unit-cell analysis is able

to predict the axial and bending stiffness coefficients (K_{11} and K_{22}) very accurately. As expected the shear stiffness (K_{33} or A_{55}) predictions have errors, but they are very minimal. It can be noticed that the corners of the unit-cell are severely deformed (Figs. 15c, 16c and 17d), when the unit-cell is subject to constant shear strain leaving the top and bottom surfaces traction free. However when shear tractions are allowed on the top and bottom surfaces of the unit-cell, the distortions at the corners disappear (Figs. 15d, 16d and 17e). Then what is obtained is the shear modulus G_{xz} and not the beam shear stiffness. The shear modulus of the plain weave beam was found to be 3.07 GPa. This would yield the apparent shear stiffness as $G_{xz}h$ =5.53 x 10^6 Nm^{-1}; whereas the actual shear stiffness is 9.21 x 10^6 Nm^{-1} (K_{33} in Table 8). The Young's modulus of the textile beam E_x may be extracted from K_{11}, as K_{11}/h, which would yield E_x = 15.42 GPa. If this value of E_x were used to predict the flexural stiffness of a homogeneous beam as $D_{11} = E_x h^3/12$, we would obtain D_{11} as 7.50 Nm—whereas the actual flexural stiffness is equal to 5.41 Nm. The same idea holds for the beam thermal coefficients also. The beam CTE's α_P, α_M and α_V cannot be predicted from the corresponding continuum CTE's. Table 9 shows the discrepancy, for the plain weave example, between the beam CTE's obtained directly and the beam CTE's obtained from the corresponding continuum CTE's. It may be noted that the continuum model would always predict the thermal expansion coefficient α_P as α_x, and the thermal bending coefficient α_M as zero. This underscores the importance of the present analysis for predicting the beam stiffness properties for a thin textile composite directly.

Table 9.   Comparison of textile CTE's.

	CTE's from beam model	CTE's from continuum model	% error
α_P x 10^{-6} /^{o}C	12.66	11.30	–10.46
α_M x 10^{-6} /^{o}C/m	–24.12	0	∞
α_V /^{o}C	0	0	0
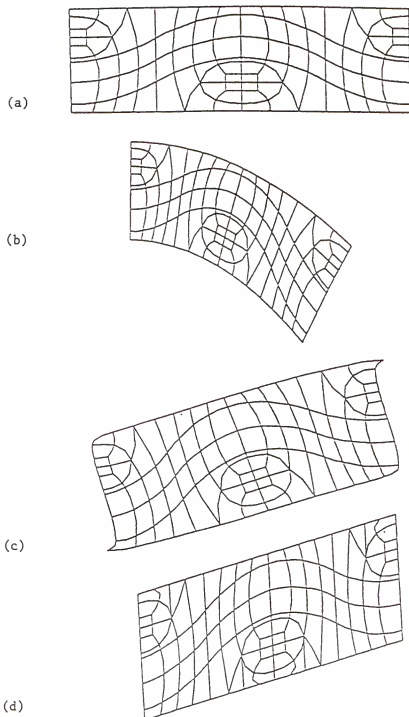
Figure 15. Deformed unit-cell of the isotropic beam. (not to scale)
(a) unit extensional strain; (b) unit curvature; (c) unit shear strain, top and
bottom surfaces are traction free; (d) unit shear strain, tractions allowed on
top and bottom surfaces.
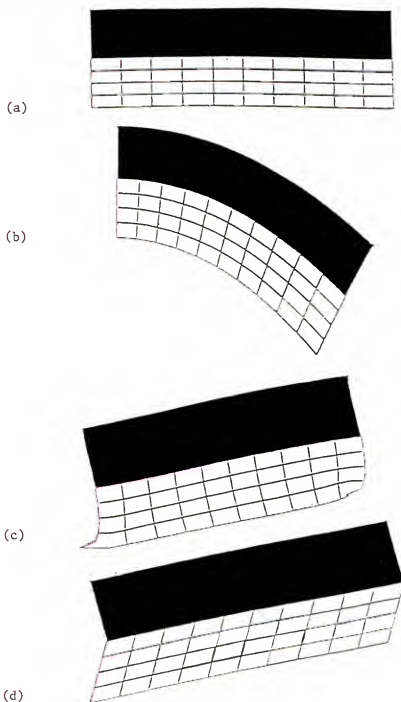
Figure 16. Deformed unit-cell of the bimaterial beam. (not to scale)
(a) unit extensional strain; (b) unit curvature; (c) unit shear strain, top and bottom surfaces are traction free; (d) unit shear strain, tractions allowed on top and bottom surfaces.
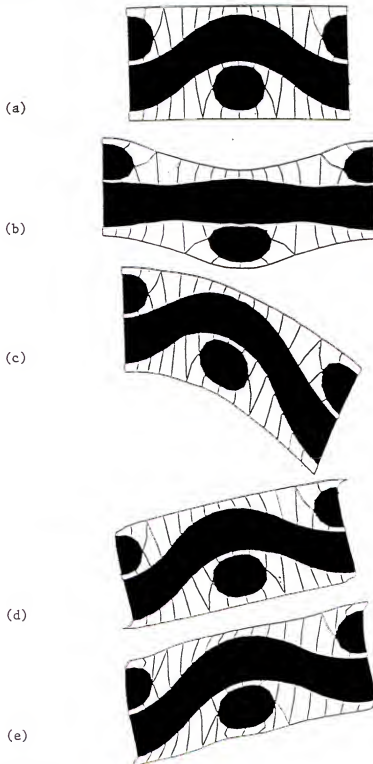
Figure 17. Textile beam. (not to scale)
(a) undeformed unit-cell; and deformation under: (b) unit extensional strain;
(c) unit curvature; (d) unit shear strain, top and bottom surfaces are traction
free; (e) unit shear strain, tractions allowed on top and bottom surfaces.

The textile beam stiffness coefficients were also estimated using a procedure similar to the mosaic model (Ishikawa and Chou, 1982a). They are compared with the coefficients obtained from the unit-cell analysis (Table 8). The idealization made in the mosaic model is shown in Figure 18. The unit cell is divided into five segments, with each segment modeled as a cross-ply laminate with a stacking sequence which best represented the yarn architecture within that segment. The stiffness matrix of each segment was computed using laminate analysis. Then the compliance of the textile beam was computed as the length-weighted average of the compliance of the five segments.

$$[S] \;=\; \left(\frac{1}{L}\right)\sum_{k=1}^{5} L^k [S]^k \qquad (21)$$

From Table 8, it can be seen that the mosaic model predicts K_{33} reasonably well. The reason for the lack of agreement in K_{11} and K_{22} can be attributed to the fact that a major portion of the yarn is modeled as a 0° laminate in the mosaic model, which tends to over-predict the axial and flexural stiffnesses.

Figure 18. Mosaic model of the textile unit-cell.
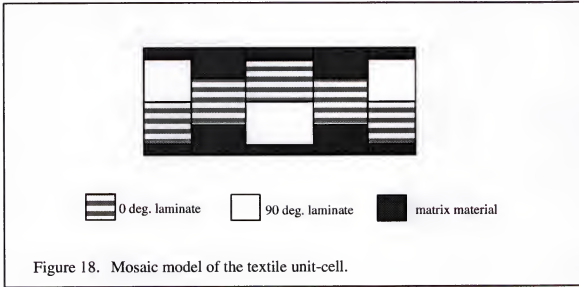
2.4 Plate Thermo-Mechanical Coefficients

The previous section described the concepts involved in modeling a thin textile composite structure as as homogeneous beam to predict the beam stiffness coefficients and CTE's. The procedure is extended in this section, utilizing three-dimensional finite element analysis, to model the thin composite as a plate (Sankar and Marrey, 1992) to determine the corresponding thermo-elastic coefficients.

The plate is assumed to be in the xy-plane with unit-cells repeating in the x- and y-directions. The lengths of the unit-cell in the x- and y-directions are assumed to be a and b respectively and the unit-cell thickness as h. On the macroscale the plate is assumed to be homogeneous and the plate behavior is characterized by the plate constitutive relation:

$$
\begin{Bmatrix} N_x \\ N_y \\ N_{xy} \\ M_x \\ M_y \\ M_{xy} \end{Bmatrix} = \begin{bmatrix} A & B \\ B & D \end{bmatrix} \left(\begin{Bmatrix} \varepsilon_{x0}^M \\ \varepsilon_{y0}^M \\ \gamma_{xy0}^M \\ \varkappa_x^M \\ \varkappa_y^M \\ \varkappa_{xy}^M \end{Bmatrix} - \begin{Bmatrix} \alpha_x^p \\ \alpha_y^p \\ \alpha_{xy}^p \\ \beta_x^p \\ \beta_y^p \\ \beta_{xy}^p \end{Bmatrix} \Delta T \right) \tag{22}
$$

where $\varepsilon_{i0}{}^M$, $\gamma_{i0}{}^M$ and $\varkappa_i{}^M$ are the midplane axial strain, shear strain and curvature; $\alpha_i{}^p$ and $\beta_i{}^p$ are the plate thermal expansion and bending coefficients; N_i and M_i are the axial force and bending moment resultants respectively in the homogeneous plate. The plate stiffness matrix comprises of the $[A]$, $[B]$ and $[D]$ sub-matrices, which are the plate extensional stiffness, coupling stiffness and bending stiffness matrices respectively. The plate stiffness

matrix can be expanded as:

$$
\begin{bmatrix} A & B \\ B & D \end{bmatrix} = \begin{bmatrix} A_{11} & A_{12} & A_{16} & B_{11} & B_{12} & B_{16} \\ A_{12} & A_{22} & A_{26} & B_{12} & B_{22} & B_{26} \\ A_{16} & A_{26} & A_{66} & B_{16} & B_{26} & B_{66} \\ B_{11} & B_{12} & B_{16} & D_{11} & D_{12} & D_{16} \\ B_{12} & B_{22} & B_{26} & D_{12} & D_{22} & D_{26} \\ B_{16} & B_{26} & B_{66} & D_{16} & D_{26} & D_{66} \end{bmatrix}
\tag{23}
$$

The midplane strains and curvatures are related to the midplane displacements and rotations as:

$$
\varepsilon_{x0}^M = \frac{\partial u_o}{\partial x}, \qquad \varepsilon_{y0}^M = \frac{\partial v_o}{\partial y}, \qquad \gamma_{xy}^M = \frac{\partial u_o}{\partial y} + \frac{\partial v_o}{\partial x}
\tag{24}
$$

$$
\varkappa_x^M = \frac{\partial \psi_x}{\partial x}, \qquad \varkappa_y^M = \frac{\partial \psi_y}{\partial y}, \qquad \varkappa_{xy}^M = \frac{\partial \psi_x}{\partial y} + \frac{\partial \psi_y}{\partial x}
\tag{25}
$$

2.4.1 Unit-Cell Boundary Conditions

The plate thermo-mechanical properties are obtained by modeling the unit-cell with eight-node brick elements and subjecting the unit-cell to six linearly independent deformations. The six deformations are given by: (1) unit ε_{x0}^M maintaining the rest of the macroscopic strains and curvatures as zero; (2) unit ε_{y0}^M such that remaining strains and curvatures are zero; and similarly (3) unit γ_{xy0}^M; (4) unit $\varkappa_x^M$; (5) unit $\varkappa_y^M$; (6) unit $\varkappa_{xy}^M$. In the last three cases (non-zero curvatures) the deformation was accompanied with a transverse deflection such that the transverse shear strain was zero (Table 10).

Table 10. Periodic displacement BC's imposed on the lateral faces of the plate unit-cell.

		$u(a,y)-$ $u(0,y)$	$v(a,y)-$ $v(0,y)$	$w(a,y)-$ $w(0,y)$	$u(x,b)-$ $u(x,0)$	$v(x,b)-$ $v(x,0)$	$w(x,b)-$ $w(x,0)$	ΔT
1.	$\varepsilon_{x0}{}^M=1$	a	0	0	0	0	0	0
2.	$\varepsilon_{y0}{}^M=1$	0	0	0	0	b	0	0
3.	$\gamma_{xy0}{}^M=1$	0	$a/2$	0	$b/2$	0	0	0
4.	$\varkappa_x{}^M=1$	az	0	$-a^2/2$	0	0	0	0
5.	$\varkappa_y{}^M=1$	0	0	0	0	bz	$-b^2/2$	0
6.	$\varkappa_{xy}{}^M=1$	0	$az/2$	$-ay/2$	$bz/2$	0	$-bx/2$	0
7.	$\Delta T^M=1$	0	0	0	0	0	0	1
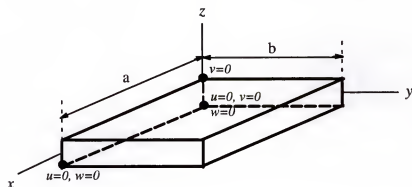
Figure 19. Boundary conditions on plate unit-cell to restrain rigid body translation and rotation.

The unit-cell is subject to minimum support constraints to prevent rigid body rotation and translation (Fig. 19). The top and bottom surfaces of the plate are assumed to be free of tractions. The faces $x=0$ and $x=a$ have identical nodes in the finite element model, and so do the pair of faces $y=0$ and $y=b$. The identical nodes on opposite faces of the unit-cell are constrained to enforce the periodic BC's. The traction boundary conditions on the lateral faces of the unit-cell are:

$$
\begin{aligned}
F_i(a, y, z) &= -F_i(0, y, z) \\
F_i(x, b, z) &= -F_i(x, 0, z)
\end{aligned} \qquad i = x, y, z \qquad (26)
$$

The periodic displacement BC's enforced for each mode of deformation are presented in Table 10.

2.4.2 Determination of Plate Stiffness Coefficients and CTE's

The six linearly independent deformations are applied to the unit-cell such that only one of the macroscopic strains or curvatures is non-zero (first six cases in Table 10). The temperature difference is set to zero for all six cases. It must be noted that the applied deformations must ensure that the transverse shear strains, γ_{xz}^{M} and γ_{yz}^{M} are zero where

$$
\begin{aligned}
\gamma_{xz}^{M} &= \psi_x + \frac{\partial w}{\partial x} \\
\gamma_{yz}^{M} &= \psi_y + \frac{\partial w}{\partial y}
\end{aligned} \qquad (27)
$$

The force and moment resultants can be obtained by one of the following two methods. In the first method, the resultants are computed by averaging the nodal forces on each face of the unit-cell. For example, on the face $x=a$ the force and moment resultants are computed using the relations:

$$
\begin{aligned}
N_x &= \left(\frac{1}{b}\right) \sum_{i=1}^{n} F_x^{(i)}(a, y, z) \\
N_{xy} &= \left(\frac{1}{b}\right) \sum_{i=1}^{n} F_y^{(i)}(a, y, z) \\
M_x &= \left(\frac{1}{b}\right) \sum_{i=1}^{n} z \, F_x^{(i)}(a, y, z) \\
M_{xy} &= \left(\frac{1}{b}\right) \sum_{i=1}^{n} z \, F_y^{(i)}(a, y, z)
\end{aligned} \qquad (28)
$$

where $F_x^{(i)}$ and $F_y^{(i)}$ are the nodal forces in the x and y directions at the ith node and $'n'$ is the total number of nodes on the face. The force and moment resultants can also be computed

by averaging the microstresses over the unit-cell volume. Then the resultants on the face $x=a$ are obtained as

$$N_x \;=\; \frac{1}{ab}\int_V \sigma_{xx}(x,y,z)\,dV \qquad N_{xy} \;=\; \frac{1}{ab}\int_V \tau_{xy}(x,y,z)\,dV \qquad (29)$$

$$M_x \;=\; \frac{1}{ab}\int_V z\sigma_{xx}(x,y,z)\,dV \qquad M_{xy} \;=\; \frac{1}{ab}\int_V z\tau_{xy}(x,y,z)\,dV \qquad (30)$$

Substituting the values of the deformation and the force resultants in the plate constitutive relation, Eqn. (22), the stiffness coefficients in the column corresponding to the non-zero deformation can be computed. This procedure is repeated for other deformation components to obtain all the stiffness coefficients.

To predict the CTE's, the plate unit-cell is subject to a uniform temperature difference, given by $\Delta T = T_0$. In the finite element model, periodic displacement BC's are applied such that all six components of the deformation are zero (seventh case in Table 10). The averaged force and moment resultants are computed using one of the procedures described above. The thermal expansion coefficients α^p, and thermal bending coefficients β^p are then obtained from the relation:

$$\left\{ \begin{array}{c} \alpha^p \\ \beta^p \end{array} \right\} \;=\; -\,\frac{1}{T_0}\left[\begin{array}{cc} A & B \\ B & D \end{array} \right]^{-1} \left\{ \begin{array}{c} N \\ M \end{array} \right\} \qquad (31)$$

2.4.3 Results for Plate Stiffness Coefficients

The plate $[A]$, $[B]$, $[D]$ matrices and CTE's were found for the seven examples listed in Table 2 by implementing the finite element code $\mu TE\chi$–10. As a preliminary check, the code was executed for an isotropic plate and compared with the plate properties using lamination theory (for one-ply). For example, A_{11} was calculated as $\dfrac{Eh}{(1 - \nu^2)}$ and D_{11} as $\dfrac{Eh^3}{12(1 - \nu^2)}$. Then the properties were computed for a bimaterial plate using the finite

element code. The plate properties for the isotropic and bimaterial cases are presented in Tables 11 and 12 respectively. The bimaterial plate properties were also computed using the lamination theory for two plies, and from the homogenous 3-D elastic constants computed in the previous section (Section 2.1). For example the coefficient D_{11} is obtained from the

3-D elastic constants as $D_{11} = \dfrac{E_x^M h^3}{12(1 - \nu_{xy}^{M^2})}$. The finite element results for the bimaterial

case were exact, *i.e.,* identical to the results obtained with the two-ply lamination theory. The [D] matrix computed from the bimaterial 3-D constants was found to be in good agreement with the two-ply lamination theory only because both the layers were equal in thickness. This is a special case, and in general, the [D] matrix obtained from the 3-D elastic constants will be different from the two-ply lamination theory results.

The plate properties for the unidirectional composite examples are presented in Table 13 and for the textile examples in Table 14. In all the examples it was found that the plate properties, especially $[B]$, D_{11}, $\{\alpha^p\}$ and $\{\beta^p\}$ could not be predicted from the corresponding 3-D elastic constants.

Table 11.   Non-zero [A], [B] and [D] coefficients for example 1 (isotropic plate) using finite elements

	A_{11} x10^6	A_{12} x10^6	A_{22} x10^6	A_{66} x10^6	D_{11} x10^{-3}	D_{12} x10^{-3}	D_{22} x10^{-3}	D_{66} x10^{-3}	α_x^p, α_y^p x10^{-6}/^{0}C
$\mu TE\chi$–10 (FEA)	2.810	0.843	2.810	0.983	15.320	4.606	15.320	5.358	10
lamination theory	2.810	0.843	2.810	0.983	15.310	4.593	15.310	5.358	10

Note: [A], [B] and [D] coefficients in SI units

Table 12. Non-zero [A], [B] and [D] coefficients for example 2 (bimaterial plate) using finite elements

	A_{11}, A_{22} x10^6	A_{12} x10^6	A_{66} x10^6	B_{11}, B_{22} x10^3	B_{12} x10^3	B_{66} x10^3
$\mu TE\chi$–10 (FEA)	9.832	2.043	3.895	– 0.563	– 0.108	– 0.228
lamination theory for two plies	9.832	2.043	3.895	– 0.563	– 0.108	– 0.228
lamination theory using 3-D elastic constants	9.844	2.048	3.899	0	0	0

	D_{11}, D_{22} x10^-3	D_{12} x10^-3	D_{66} x10^-3	α_x^P, α_y^P x10^-6 /°C	β_x^P, β_y^P /°C/m
$\mu TE\chi$–10 (FEA)	53.590	11.149	21.220	17.800	0.170
lamination theory for two plies	53.573	11.131	21.220	17.814	0.170
lamination theory using 3-D elastic constants	53.762	11.183	21.293	8.190	0

Note: [A], [B] and [D] coefficients in SI units

Table 13. Non-zero [A], [B] and [D] coefficients for examples 3 and 4 (unidirectional composite) using finite elements

		A_{11} x10^6	A_{12} x10^6	A_{22} x10^6	A_{66} x10^6
Example 3	$\mu TE\chi$–10 (FEA)	0.690	0.149	0.496	0.177
	Halpin-Tsai Eqns. and lamination theory	0.673	0.109	0.363	0.113
Example 4	$\mu TE\chi$–10 (FEA)	0.452	0.062	0.285	0.114
	Halpin-Tsai Eqns. and lamination theory	0.444	0.039	0.151	0.045

		D_{11} x10^{-6}	D_{12} x10^{-6}	D_{22} x10^{-6}	D_{66} x10^{-6}	$a_x{}^p$x 10^{-6}	$a_y{}^p$x 10^{-6}
Example 3	$\mu TE\chi$–10 (FEA)	3.589	0.596	1.980	0.947	15.489	26.184
	Halpin-Tsai Eqns. and lamination theory	5.606	0.908	3.026	0.939	15.625	55.112
Example 4	$\mu TE\chi$–10 (FEA)	2.256	0.224	0.873	0.568	7.378	13.188
	Halpin-Tsai Eqns. and lamination theory	3.702	0.328	1.262	0.371	6.774	34.239

Note: [A], [B] and [D] coefficients in SI units

Table 14. Non-zero [A], [B] and [D] coefficients for examples 5, 6 and 7 using finite elements

		A_{11}, A_{22} x10^6	A_{12} x10^6	A_{66} x10^6	B_{11} x10^3
Example 5	$\mu TE\chi$–10 (FEA)	2.681	0.565	0.489	0
	lamination theory using 3-D constants	2.783	0.503	0.490	0
Example 6	$\mu TE\chi$–10 (FEA)	12.090	3.470	1.223	0
	lamination theory using 3-D constants	13.938	1.787	1.208	0
Example 7	$\mu TE\chi$–10 (FEA)	14.683	1.351	1.210	0.495*
	lamination theory using 3-D constants	16.531	0.770	1.239	0

		D_{11}, D_{22} x10^{-3}	D_{12} x10^{-3}	D_{66} x10^{-3}	$\alpha_x{}^p, \alpha_y{}^p$ x10^{-6} /°C	$\beta_x{}^p$ /°C/m
Example 5	$\mu TE\chi$–10 (FEA)	5.687	1.518	1.577	27.465	0
	lamination theory using 3-D constants	12.054	2.177	2.124	28.363	0
Example 6	$\mu TE\chi$–10 (FEA)	41.695	0.373	5.879	1.480	0
	lamination theory using 3-D constants	75.942	9.734	6.582	1.556	0
Example 7	$\mu TE\chi$–10 (FEA)	90.072	1.123	6.149	2.910	–0.037*
	lamination theory using 3-D constants	87.283	4.195	6.753	1.550	0

* In example 7, $B_{22} = -B_{11}$ and $\beta_y{}^p = -\beta_x{}^p$

Note: [A], [B] and [D] coefficients in SI units

CHAPTER 3
ANALYTICAL MODELS FOR THERMO-ELASTIC CONSTANTS

The complex yarn architectures in a textile composite make numerical modeling of the unit-cell extremely difficult. Besides, the computational memory and run-time requirements for a detailed finite element analysis are enormous. As explained in the introductory chapter, there are several parameters that can be changed to alter the effective composite properties. These parameters may be the fiber material in the yarn, fiber volume fraction in the yarn (also called yarn packing density), overall fiber volume fraction, preform architecture or the matrix material properties. This emphasizes the need for simple analysis procedures to predict the trend in variation of composite properties when one of the parameters is changed. These procedures will be of use to a designer in determining the optimum parameters for a certain application.

Analytical methods are approximate because they assume certain forms for the state of stress and strain in the unit-cell. Averaging the stiffnesses or compliances of the matrix and the inclusion has long been used to estimate the bounds of effective elastic properties of the composite. Essentially the stiffness averaging assumes a state of uniform strain in the composite (isostrain), and compliance averaging assumes a state of uniform stress (isostress) in the matrix and inclusion. In fact the rule of mixtures expressions for estimating the effective properties of a unidirectional composite is based on such averaging schemes. Naik (1994) proposed an analytical method (TEXCAD) in which the yarns are discretized into segments. Knowing the direction of the yarn in each segment, the segment stiffness are computed using appropriate transformations. Then assuming a state of isostrain, the composite stiffness is obtained by volume-averaging the yarn-segment stiffness and matrix stiffness in the unit-cell. This method seems to work, when there is multi-directional

reinforcement in the composite. However the method fails for composites with preferential yarn reinforcement. For example, the transverse modulus and the inplane shear modulus for a unidirectional composite cannot be estimated using the above method. Another analytical model called the mosaic model, was proposed by Ishikawa and Chou (1982a). As discussed earlier, in the mosaic model the yarn architecture is simplified to that of a cross-ply laminate and the lamination theory is used to predict the composite properties.

The state of stress/strain in a textile composite, subjected to a uniform macrostress, is much more complex than that assumed in the above mentioned methods. We propose a scheme of selective averaging—called the selective averaging method (SAM)—in which both stiffness and compliance coefficients can be averaged selectively depending on a more realistic assumption of either isostress or isostrain.

3.1 Selective Averaging Method (SAM) for Continuum Properties

In this section, we describe SAM for estimating the effective elastic constants and CTE's for a textile composite. Consider a rectangular hexahedron of dimensions $a \times b \times c$ as the unit-cell. The unit-cell is discretized into slices on the mesoscale, and elements on the microscale as shown in Fig. 20. To distinguish between the macrolevel, mesolevel and microlevel properties in this section, an over-tilde is used to denote the mesolevel properties, and a superscript "M" is used to denote the macrolevel properties. For example, $[C^M]$, $[\tilde{C}]$ and $[C]$ will represent the macrolevel, mesolevel and microlevel stiffnesses respectively.

The objective here is to determine the coefficients of the effective stiffness matrix $[C^M]$ as defined in Eqn. (2). To find the first column of the effective stiffness matrix, the unit-cell is divided into slices (mesolevel) of thickness dx parallel to the yz-plane (Fig. 20a). Each slice is further sub-divided into elements (microlevel) as shown in Figs. 20(b) and 20(c). The unit-cell is subjected to a deformation such that all macrostrains except ε_{xx}^M are equal to zero and $\varepsilon_{xx}^M = 1$. It is assumed that the mesolevel and microlevel strains,

corresponding to the zero macrostrains, are negligible. In other words,

$$\varepsilon_i^M \ = \ \tilde{\varepsilon}_i \ = \ \varepsilon_i \ = \ 0 \qquad\qquad i \neq 1 \qquad\qquad (32)$$
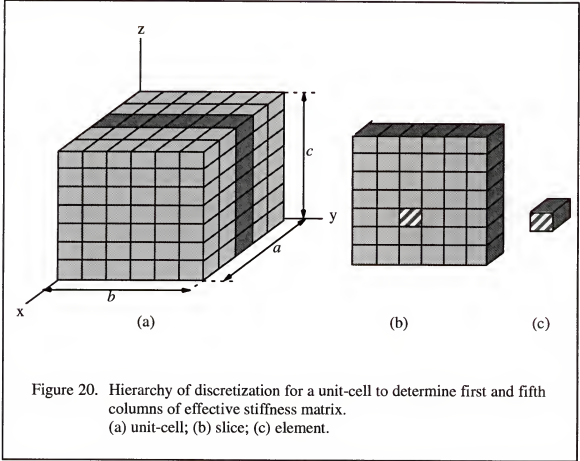
Figure 20. Hierarchy of discretization for a unit-cell to determine first and fifth columns of effective stiffness matrix.
(a) unit-cell; (b) slice; (c) element.

Assuming a state of isostrain within the slice ($\varepsilon_{xx}(x,y,z) = \tilde{\varepsilon}(x)$) the average stiffness of a slice can be obtained as:

$$\tilde{C}_{11}(x) \ = \ \frac{1}{bc} \int\limits_{z=0}^{c} \int\limits_{y=0}^{b} C_{11}(x,y,z) \ dy \ dz \qquad\qquad (33)$$

where $C_{11}(x,y,z)$ is the element stiffness coefficient referred to the unit-cell coordinates. The stiffnesses of the slices are averaged on the macrolevel based on the isostress assumption, *i.e.*, $\tilde{\sigma}_{xx}(x) = \sigma_{xx}^M$. Then the first column of the effective stiffness matrix can be computed using the following two relations:

$$\frac{1}{C_{11}^M} = \frac{1}{a} \int\limits_{x=0}^{a} \frac{1}{\tilde{C}_{11}(x)} dx \tag{34}$$

$$C_{i1}^M = \frac{1}{abc} \int\limits_{z=0}^{c} \int\limits_{y=0}^{b} \int\limits_{x=0}^{a} \frac{C_{11}^M}{\tilde{C}_{11}(x)} \, C_{i1}(x,y,z) \, dx \, dy \, dz \quad (i = 2,\ldots,6) \tag{35}$$

A similar procedure can be implemented to determine the second and third columns of the macroscale stiffness matrix $[C^M]$.

A slightly different averaging scheme is used when the unit-cell is subjected to shear strains on the macrolevel. Consider the case where the unit-cell is subjected to unit γ_{yz} at macroscale. The unit-cell is again discretized into slices and elements as shown in Fig. 20. It is assumed that all the other components of strain at the macrolevel, mesolevel and microlevels are zero. This can be expressed as:

$$\varepsilon_i^M = \bar{\varepsilon}_i = \varepsilon_i = 0 \qquad i \neq 4 \tag{36}$$

where $\varepsilon_4 = \gamma_{yz}$. We also assume that the shear stress is constant in a slice such that $\tau_{yz}(x,y,z) = \bar{\tau}_{yz}(x)$. The shear compliance of a slice can then be obtained by averaging the shear compliances of all the elements in the slice as:

$$\frac{1}{\tilde{C}_{44}(x)} = \frac{1}{bc} \int\limits_{z=0}^{c} \int\limits_{y=0}^{b} \frac{1}{C_{44}(x,y,z)} dy \, dz \tag{37}$$

The fourth column of the stiffness matrix $C_{i4}{}^M$ is obtained under the assumption that all the slices are under a state of constant shear strain:

$$C_{i4}^M = \frac{1}{abc} \int\limits_{z=0}^{c} \int\limits_{y=0}^{b} \int\limits_{x=0}^{a} \frac{\tilde{C}_{44}(x)}{C_{44}(x,y,z)} \, C_{i4}(x,y,z) \, dx \, dy \, dz \quad (i = 1,\ldots,6) \tag{38}$$

A similar procedure is used to determine the fifth and sixth columns of $[C^M]$.

To determine the macroscale CTE's, a uniform temperature difference (ΔT) is applied throughout the unit-cell. The unit-cell is constrained from expanding such that all the strain components on the macrolevel are zero. A state of isostrain is assumed in the unit-cell, implying that the mechanical strain components on the mesolevel and microlevel are also zero. This can be expressed as:

$$\varepsilon_i^M = \tilde{\varepsilon}_i = \varepsilon_i = 0 \qquad i = 1,\ldots,6 \tag{39}$$

Then the thermal constitutive relations on the macrolevel and microlevel will reduce to:

$$\begin{aligned} \{\sigma^M\} &= -[C^M]\{\alpha^c\}\Delta T \\ \{\sigma\} &= -[C]\{\alpha\}\Delta T \end{aligned} \tag{40}$$

The macrostresses may be computed by volume-averaging the corresponding microstress component as shown below:

$$\{\sigma^M\} = \frac{1}{abc} \int\limits_{z=0}^{c} \int\limits_{y=0}^{b} \int\limits_{x=0}^{a} \{\sigma\} \; dx \; dy \; dz \tag{41}$$

Then from Eqns. (40) and (41), we can compute the macroscale CTE's as:

$$\{\alpha^c\} = \frac{1}{abc} [C^M]^{-1} \{I\} \tag{42}$$

where $\{I\}$ is given by the expression:

$$\{I\} = \int\limits_{z=0}^{c} \int\limits_{y=0}^{b} \int\limits_{x=0}^{a} [C]\{\alpha\} \; dx \; dy \; dz \tag{43}$$

3.2 Continuum Results using SAM

A code called $\mu TE\chi$–20 (pronounced as *microtech*) was written in FORTRAN 77 to implement SAM. The code was executed to estimate the thermo-elastic constants for the seven examples, whose constituent material properties are listed in Table 1. Input to the code were the unit-cell dimensions, yarn geometry information, constituent material properties,

and the number of divisions required to discretize the unit-cell in the x, y and z directions. The element stiffness matrix $[C]$ was determined by computing the elasticity matrix for the material point at the geometric center of the element, and transforming it to the unit-cell coordinate system. The predicted macroscale stiffness matrix $[C^M]$, and consequently the macroscale compliance matrix will not be symmetric due to the approximate nature of the analysis. Therefore the macroscale compliance matrix was made symmetric by averaging the off-diagonal compliance coefficients. The macroscale elastic constants were computed by comparing the symmetrized compliance coefficients with that of a homogenous, orthotropic medium.

The results for a bimaterial medium (example 2) are given in Table 15. The results for example 1 are not listed, since it is obvious that SAM would predict the elastic constants for an isotropic medium exactly. The bimaterial medium consisted of two different layers of isotropic materials of equal thickness alternatingly stacked in the z-direction. The elastic constants for the bimaterial medium were compared with an exact solution (derivation explained in Section 2.1.3), and with the previously computed finite element results. It can be observed that SAM marginally under-predicts the longitudinal and transverse Young's moduli, while the inplane and transverse shear moduli are exact.

Table 15.   Continuum properties for example 2 using SAM.

		E_x, E_y (GPa)	E_z (GPa)	$G_{xz},$ G_{yz} (GPa)	G_{xy} (GPa)	$\nu_{xz},$ ν_{yz}	ν_{xy}	$\alpha_x{}^c, \alpha_y{}^c$ x $10^{-6}/{}^oC$	$\alpha_z{}^c$ x $10^{-6}/{}^oC$
Example 2 (bimaterial medium)	$\mu TE\chi$–20 (SAM)	36.02	8.72	2.48	15.23	0.599	0.183	3.88	52.20
	$\mu TE\chi$–10 (FEA)	36.79	9.79	2.48	15.23	0.312	0.208	8.19	59.60
	exact solution	36.79	9.79	2.48	15.23	0.312	0.208	8.19	59.60

Table 16 presents the SAM results for two cases of unidirectional composite (examples 3 and 4). The fiber and matrix had identical Poisson's ratio in example 3, and different Poisson's ratio in example 4. The SAM results were compared with the finite element results from the previous chapter, and with analytical solutions for unidirectional composite properties. The analytical expressions used were the rule of mixtures formulae for E_L and ν_{LT} and the Halpin-Tsai equations (Halpin and Tsai, 1969) for E_T, G_{LT} and ν_{TT}. All of the unidirectional composite thermo-elastic constants but for E_T and α_T were found to match well with the compared data. Table 17 compares the SAM results for three textile composites (examples 5, 6 and 7) with available results. In all three cases the thermo-elastic constants obtained by implementing SAM were in good agreement with the available results.

Table 16.   Continuum properties for examples 3 and 4 using SAM.

		E_L (GPa)	E_T (GPa)	G_{LT} (GPa)	G_{TT} (GPa)	ν_{LT}	ν_{TT}	α_L x 10^{-6} /°C	α_T x10^{-6} /°C
Example 3 (unidirect. composite)	$\mu TE\chi$–20 (SAM)	64	50.24	10.45	8.36	0.341	0.300	12.41	21.51
	$\mu TE\chi$–10 (FEA)	63.55	36.48	12.93	9.94	0.300	0.232	15.74	40.79
	rule of mixt./ Halpin– Tsai eqns.	64	34.55	11.26	13.29	0.300	0.300	15.63	55.11
Example 4 (unidirect. composite)	$\mu TE\chi$–20 (SAM)	43.35	32.47	4.13	3.04	0.245	0.218	7.40	11.60
	$\mu TE\chi$–10 (FEA)	43.12	18.15	5.59	3.92	0.242	0.222	7.40	25.44
	rule of mixt./ Halpin– Tsai eqns.	43.40	14.79	4.45	5.91	0.260	0.252	6.77	34.24

Table 17.　Continuum properties for examples 5, 6 and 7 using SAM.

		E_x, E_y (GPa)	E_z (GPa)	G_{xz}, G_{yz} (GPa)	G_{xy} (GPa)	ν_{xz}, ν_{yz}	ν_{xy}	$\alpha_x{}^c, \alpha_y{}^c x$ $10^{-6}/^oC$	$\alpha_z{}^c x$ $10^{-6}/^oC$
Example 5 (plain-weave)	$\mu TE\chi$–20 (SAM)	12.46	6.62	1.64	1.67	0.399	0.162	29.10	68.48
	$\mu TE\chi$–10 (FEA)	11.81	6.14	1.84	2.15	0.408	0.181	28.36	79.57
	Dasgupta results	14.38	6.25	1.94	3.94	0.463	0.167	22.50	86.00
Example 6 (plain-weave)	$\mu TE\chi$–20 (SAM)	63.41	11.13	3.79	4.24	0.402	0.027	1.36	21.53
	$\mu TE\chi$–10 (FEA)	53.61	10.88	4.41	4.72	0.365	0.128	1.56	22.71
	TEXCAD	64.38	11.49	5.64	4.87	0.396	0.027	1.33	20.71
Example 7 (5–harness weave)	$\mu TE\chi$–20 (SAM)	69.30	11.62	4.06	4.73	0.355	0.031	1.21	20.25
	$\mu TE\chi$–10 (FEA)	64.51	11.33	4.45	4.85	0.329	0.047	1.55	22.03
	TEXCAD	66.33	11.51	4.93	4.89	0.342	0.034	1.46	21.24

3.3 Selective Averaging Method (SAM) for Plate Properties

In this section, the SAM procedure to compute the plate stiffness coefficients and plate thermal coefficients (for a thin textile composite) is described. To distinguish between the macrolevel, mesolevel and microlevel [A], [B] and [D] matrices, an over-tilde is used to denote the mesolevel stiffness, and a superscript "M" is used to denote the macrolevel plate stiffness. However in the remaining sections, [A], [B] and [D] (without a superscript or overscript) will refer to the macroscale plate stiffness matrices. Also in this section, the

complete plate stiffness matrix on the macroscale, as defined by Eqn. (23) will be denoted by $[C^M]$, such that:

$$[C^M] = \begin{bmatrix} A^M & B^M \\ B^M & D^M \end{bmatrix} \tag{44}$$

The procedure to find the plate stiffness and thermal coefficients is analogous to that used to find the continuum thermo-elastic constants. To find the first column of the effective plate stiffness matrix, the unit-cell is discretized into slices (mesolevel) and elements (microlevel) as shown in Fig. 20. The unit-cell is subject to the deformation given by $\varepsilon_{x0}^M = 1$. The following assumptions are made regarding the midplane strains and curvatures on the macrolevel, mesolevel and microlevel:

$$\begin{aligned} \varepsilon_{i0}^M &= \tilde{\varepsilon}_{i0} = \varepsilon_{i0} = 0 \qquad i = 2, 3 \\ \varkappa_i^M &= \tilde{\varkappa}_i = \varkappa_i = 0 \qquad i = 1, 3 \end{aligned} \tag{45}$$

It is also assumed that the non-zero strain component ε_{x0}, and the force resultant N_x are uniform within the mesoscale and macroscale respectively. These two assumptions can be expressed as the following equations:

$$\begin{aligned} \varepsilon_{x0} &= \tilde{\varepsilon}_{x0} \\ \tilde{N}_x &= N_x^M \end{aligned} \tag{46}$$

The mesolevel stiffness coefficient $\tilde{A}_{11}$ can then be obtained by averaging the corresponding element stiffness coefficients over the slice (consequence of the isostrain assumption) as:

$$\tilde{A}_{11}(x) = \frac{1}{b} \int_{z=0}^{c} \int_{y=0}^{b} Q_{11}(x, y, z) \ dy \ dz \tag{47}$$

where Q_{11} is the plane-stress stiffness coefficient in the classical lamination theory (Agarwal and Broutman, 1990), which has been transformed to the unit-cell's xyz-coordinates (for an

isotropic material, $Q_{11} = \dfrac{E}{(1 - \nu^2)}$). The macroscale force and moment resultants can be expressed in terms of the microscale stresses by the following relations:

$$N_i^M = \frac{1}{ab} \int\limits_{z=0}^{c} \int\limits_{y=0}^{b} \int\limits_{x=0}^{a} \sigma_i \, dx \, dy \, dz$$

$$i = 1, 2, 3 \qquad (48)$$

$$M_i^M = \frac{1}{ab} \int\limits_{z=0}^{c} \int\limits_{y=0}^{b} \int\limits_{x=0}^{a} z \, \sigma_i \, dx \, dy \, dz$$

The assumption of uniform force resultants on the macroscale and Eqn. (48) yields the following expressions for the first column of plate stiffness coefficients:

$$\frac{1}{A_{11}^M} = \frac{1}{a} \int\limits_{x=0}^{a} \frac{1}{\tilde{A}_{11}(x)} dx \qquad (49)$$

$$C_{i1}^M = \frac{1}{ab} \int\limits_{z=0}^{c} \int\limits_{y=0}^{b} \int\limits_{x=0}^{a} \frac{A_{11}^M}{\tilde{A}_{11}(x)} \, Q_{i1}(x,y,z) \, dx \, dy \, dz \quad (i = 1, 2, 3) \qquad (50)$$

$$C_{j1}^M = \frac{1}{ab} \int\limits_{z=0}^{c} \int\limits_{y=0}^{b} \int\limits_{x=0}^{a} z \, \frac{A_{11}^M}{\tilde{A}_{11}(x)} \, Q_{i1}(x,y,z) \, dx \, dy \, dz \quad \begin{matrix} (i = 1, 2, 3) \\ j = i + 3 \end{matrix} \qquad (51)$$

A similar procedure is followed to compute the second column of the effective plate stiffness matrix.

In the case of shear loading $\gamma_{xy}^M = 1$, the unit-cell is discretized into slices parallel to the yz-plane. The assumptions of isostrain and uniform force resultants are reversed from the case of normal loading. The force resultant N_{xy} is assumed to be uniform within a slice, such that

$$\tilde{N}_{xy} = N_{xy} \qquad (52)$$

It is also assumed that γ_{xy} is the only non-zero deformation component on the macrolevel, mesolevel and microlevel. Averaging the element compliance coefficients over the slice, we obtain:

$$\frac{1}{\bar{Q}_{33}(z)} = \frac{1}{ab} \int\limits_{y=0}^{b} \int\limits_{x=0}^{a} \frac{1}{Q_{33}(x,y,z)} \; dx \; dy \tag{53}$$

The mesolevel stiffnesses are then averaged over the volume of the unit-cell to yield the third column of the plate stiffness matrix, as follows

$$C_{i3}^{M} = \frac{1}{ab} \int\limits_{z=0}^{c} \int\limits_{y=0}^{b} \int\limits_{x=0}^{a} \frac{Q_{i3}(x,y,z)}{Q_{33}(x,y,z)} \; \bar{Q}_{33}(z) \; dx \; dy \; dz \quad (i = 1,2,3) \tag{54}$$

$$C_{j3}^{M} = \frac{1}{ab} \int\limits_{z=0}^{c} \int\limits_{y=0}^{b} \int\limits_{x=0}^{a} z \frac{Q_{i3}(x,y,z)}{Q_{33}(x,y,z)} \; \bar{Q}_{33}(z) \; dx \; dy \; dz \quad \begin{array}{l} (i = 1,2,3) \\ j = i + 3 \end{array} \tag{55}$$

The expressions for the fourth, fifth and sixth columns of the plate stiffness matrix can be obtained in a similar fashion to that explained above, except that the one of the curvature component will be non-zero instead of a midplane strain component. For example, to determine the fourth column, $\varkappa_{x}$ will be the only non-zero deformation on the macroscale, mesoscale and microscale. Assuming that the curvature is uniform within a slice, we get $\varkappa_{x} = \bar{\varkappa}_{x}$. Then by averaging the element stiffness coefficients over the slice, we obtain an expression analogous to Eqn. (47) as:

$$\tilde{D}_{11}(x) = \frac{1}{b} \int\limits_{z=0}^{c} \int\limits_{y=0}^{b} z^2 Q_{11}(x,y,z) \; dy \; dz \tag{56}$$

The moment resultant M_x is assumed to be uniform on the mesoscale such that $M_x^{M} = \bar{M}_x$. By averaging the slice compliance coefficients over the unit-cell volume, we get the following relations for the fourth column of the plate stiffness matrix:

$$\frac{1}{D_{11}^M} = \frac{1}{a} \int_{x=0}^{a} \frac{1}{\tilde{D}_{11}(x)} dx \tag{57}$$

$$C_{i4}^M = \frac{1}{ab} \int_{z=0}^{c} \int_{y=0}^{b} \int_{x=0}^{a} z \frac{D_{11}^M}{\tilde{D}_{11}(x)} Q_{i1}(x,y,z) \, dx \, dy \, dz \quad (i = 1,2,3) \tag{58}$$

$$C_{j4}^M = \frac{1}{ab} \int_{z=0}^{c} \int_{y=0}^{b} \int_{x=0}^{a} z^2 \frac{D_{11}^M}{\tilde{D}_{11}(x)} Q_{i1}(x,y,z) \, dx \, dy \, dz \quad \begin{matrix} (i = 1,2,3) \\ j = i+3 \end{matrix} \tag{59}$$

The fifth and sixth columns of the plate stiffness matrix can be found by using a similar procedure.

To find the plate thermal coefficients, ε_{i0} and $\varkappa_i$ are assumed as zero in the macrolevel, mesolevel and microlevel. The thermal stresses developed in the microscale due to a uniform temperature difference of $\Delta T = T_0$ are given by:

$$\{\sigma\} = -[Q]\{\alpha\}T_0 \tag{60}$$

where

$$\{\sigma\} = \begin{Bmatrix} \sigma_x \\ \sigma_y \\ \tau_{xy} \end{Bmatrix} \qquad \{\alpha\} = \begin{Bmatrix} \alpha_x \\ \alpha_y \\ \alpha_{xy} \end{Bmatrix} \tag{61}$$

The macroscale plate constitutive equation will reduce to

$$\begin{Bmatrix} N^M \\ M^M \end{Bmatrix} = -[C^M] \begin{Bmatrix} \alpha^p \\ \beta^p \end{Bmatrix} T_0 \tag{62}$$

By averaging the microscale stresses given by Eqn. (60) over the unit-cell volume (using Eqn. 48), and equating to the macroscale force and moment resultants in Eqn. (62), we get the following relations for the plate CTE's:

$$\begin{Bmatrix} \alpha^p \\ \beta^p \end{Bmatrix} = [C^M]^{-1} \begin{Bmatrix} I_1 \\ I_2 \end{Bmatrix} \tag{63}$$

where I_1 and I_2 are integrals given by the expressions:

$$I_1 = \frac{1}{ab} \int\limits_{z=0}^{c} \int\limits_{y=0}^{b} \int\limits_{x=0}^{a} [Q]\{\alpha\} \ dx \ dy \ dz$$

(64)

$$I_2 = \frac{1}{ab} \int\limits_{z=0}^{c} \int\limits_{y=0}^{b} \int\limits_{x=0}^{a} z \ [Q]\{\alpha\} \ dx \ dy \ dz$$

3.4 Plate Results using SAM

The plate coefficients and plate CTE's were computed for examples 2-7 by implementing SAM, and compared with the finite element results presented in the previous chapter. The computed coefficients for the examples are listed in Tables. 18-20. The properties for the bimaterial plate were predicted very accurately (Table 18). For the unidirectional composite examples, SAM was able to predict the $[A]$ matrix coefficients (except for A_{66}), D_{11}, and the plate CTE's very well (Table 19). However SAM grossly over-predicted D_{12} and D_{22} and under-predicted the coefficient D_{66}. For the textile composite examples (Table 20) SAM predicted all but A_{12} and D_{12} with very good accuracy.

Table 18. Non-zero [A], [B] and [D] coefficients for example 2 (bimaterial plate) using SAM.

	A_{11}, A_{22} x10^6	A_{12} x10^6	A_{66} x10^6	B_{11}, B_{22} x10^3	B_{12} x10^3	B_{66} x10^{-3}
$\mu TE\chi$–20 (SAM)	9.844	2.045	3.899	– 0.565	– 0.108	– 0.228
$\mu TE\chi$–10 (FEA)	9.832	2.043	3.895	– 0.563	– 0.108	– 0.228
lamination theory for two plies	9.832	2.043	3.895	– 0.563	– 0.108	– 0.228
lamination theory using 3-D elastic constants	9.844	2.048	3.899	0	0	0

	D_{11}, D_{22} x10^{-3}	D_{12} x10^{-3}	D_{66} x10^{-3}	$\alpha_x{}^p, \alpha_y{}^p$ x10^{-6} /^{o}C	$\beta_x{}^p, \beta_y{}^p$ /^{o}C/m
$\mu TE\chi$–20 (SAM)	53.727	11.163	21.282	17.828	0.170
$\mu TE\chi$–10 (FEA)	53.590	11.149	21.220	17.800	0.170
lamination theory for two plies	53.573	11.131	21.220	17.814	0.170
lamination theory using 3-D elastic constants	53.762	11.183	21.293	8.190	0

Note: [A], [B] and [D] coefficients in SI units

Table 19. Non-zero [A], [B] and [D] coefficients for examples 3 and 4 (unidirectional composite) using SAM.

		A_{11} x10^6	A_{12} x10^6	A_{22} x10^6	A_{66} x10^6
Example 3	$\mu TE\chi$–20 (SAM)	0.688	0.175	0.475	0.102
	$\mu TE\chi$–10 (FEA)	0.690	0.149	0.496	0.177
	Halpin-Tsai Eqns. and lamination theory	0.673	0.109	0.363	0.113
Example 4	$\mu TE\chi$–20 (SAM)	0.443	0.074	0.261	0.040
	$\mu TE\chi$–10 (FEA)	0.452	0.062	0.285	0.114
	Halpin-Tsai Eqns. and lamination theory	0.444	0.039	0.151	0.045

		D_{11} x10^{-6}	D_{12} x10^{-6}	D_{22} x10^{-6}	D_{66} x10^{-6}	$\alpha_x{}^P$x 10^{-6}	$\alpha_y{}^P$x 10^{-6}
Example 3	$\mu TE\chi$–20 (SAM)	3.750	1.029	3.112	0.541	14.476	24.750
	$\mu TE\chi$–10 (FEA)	3.589	0.596	1.980	0.947	15.489	26.184
	Halpin-Tsai Eqns. and lamination theory	5.606	0.908	3.026	0.939	15.625	55.112
Example 4	$\mu TE\chi$–20 (SAM)	2.308	0.446	1.799	0.195	6.628	13.076
	$\mu TE\chi$–10 (FEA)	2.256	0.224	0.873	0.568	7.378	13.188
	Halpin-Tsai Eqns. and lamination theory	3.702	0.328	1.262	0.371	6.774	34.239

Note: [A], [B] and [D] coefficients in SI units

Table 20.   Non-zero [A], [B] and [D] coefficients for examples 5, 6 and 7 using SAM.

		A_{11}, A_{22} x 10^6	A_{12} x 10^6	A_{66} x 10^6	B_{11} x10^3
Example 5	$\mu TE\chi$–20 (SAM)	2.667	0.446	0.379	0
	$\mu TE\chi$–10 (FEA)	2.681	0.565	0.489	0
	lamination theory using 3-D constants	2.783	0.503	0.490	0
Example 6	$\mu TE\chi$–20 (SAM)	12.215	0.577	1.095	0
	$\mu TE\chi$–10 (FEA)	12.090	3.470	1.223	0
	lamination theory using 3-D constants	13.938	1.787	1.208	0
Example 7	$\mu TE\chi$–20 (SAM)	16.039	0.631	1.209	0.590*
	$\mu TE\chi$–10 (FEA)	14.683	1.351	1.210	0.495*
	lamination theory using 3-D constants	16.531	0.770	1.239	0

		D_{11}, D_{22} x 10^{-3}	D_{12} x 10^{-3}	D_{66} x 10^{-3}	$\alpha_x{}^p, \alpha_y{}^p$ x 10^{-6}/°C	$\beta_x{}^p$ /°C/m
Example 5	$\mu TE\chi$–20 (SAM)	6.017	1.590	1.360	27.505	0
	$\mu TE\chi$–10 (FEA)	5.687	1.518	1.577	27.465	0
	lamination theory using 3-D constants	12.054	2.177	2.124	28.363	0
Example 6	$\mu TE\chi$–20 (SAM)	44.782	2.733	4.398	1.984	0
	$\mu TE\chi$–10 (FEA)	41.695	0.373	5.879	1.480	0
	lamination theory using 3-D constants	75.942	9.734	6.582	1.556	0
Example 7	$\mu TE\chi$–20 (SAM)	81.164	3.307	5.868	2.422	–0.028*
	$\mu TE\chi$–10 (FEA)	90.072	1.123	6.149	2.910	–0.037*
	lamination theory using 3-D constants	87.283	4.195	6.753	1.550	0

* In example 7, $B_{22} = -B_{11}$ and $\beta_y{}^p = -\beta_x{}^p$

Note: [A], [B] and [D] coefficients in SI units

CHAPTER 4
FINITE ELEMENT MODELS FOR STRENGTH PROPERTIES

In Chapter 2, we had demonstrated finite element procedures to model a general textile composite either as a three-dimensional (continuum) material or as a thin plate/beam to predict their corresponding thermo-mechanical coefficients. In this chapter, we extend the same numerical models to compute the thermal residual stresses due to processing in the yarns and the matrix. Then the numerical models are used to study the strength behavior of the composite by predicting the failure envelopes for thin and thick textile composites.

4.1 Thermally Induced Residual Microstresses

The thermal residual microstresses are induced in the yarn and matrix materials due to the mismatch in their corresponding CTE's. The difference between the composite curing temperature and room temperature then serves as the driving force to create these microstresses. Since composites designed for high temperature applications are fabricated at higher temperatures, the residual microstresses become relevant in the strength considerations of such composites. The residual microstresses in the vicinity of the yarn-matrix interface are particularly important as they could lead to failure due to debonding.

Determination of residual microstresses. Let T_o be the difference between room temperature and the composite fabrication temperature. Since the composite is stress free at the fabrication temperature, which is above room temperature, T_o is generally negative. The residual microstresses in the yarn and the matrix are obtained by superposing the microstresses due to the two load cases as explained below. In the first load case, the unit-cell

is constrained from expanding by fixing the corner nodes of the unit-cell and enforcing zero displacement difference between corresponding nodes on opposite faces of the unit-cell (periodic displacement BC's). A temperature difference T_o is applied to all elements in the finite element model. This is exactly the same problem we solve for finding the three-dimensional (continuum) CTE's. The applied boundary conditions mean that all the macrostrain components are equal to zero ($\{\varepsilon^M\} = 0$, $\Delta T^M = T_0$). Then the corresponding macrostresses required to restrain the unit-cell expansion are given by:

$$\{\sigma^M\} = -[C]\{a^c\}T_o \tag{65}$$

In the second load case, deformations are applied so as to reverse the macrostresses developed in the first load case. This can be accomplished by imposing the deformations $\{\varepsilon^M\} = \{a^c\}\ T_o$ and $\Delta T^M = 0$. It can be noted that the macrostresses developed in the second loading case, given by $[C]\{a^c\}T_o$ are equal and opposite to the macrostresses in Eqn. (65). The microstresses from both load cases are superposed to obtain the residual stresses due to free thermal expansion.

The same idea can be extended to finding the residual microstresses in the plate model. Then the deformations to be applied in the first load case are $\{\varepsilon_0^M\} = 0$, $\{\varkappa^M\} = 0$ and $\Delta T^M = T_o$; and the deformations in the second load case are $\{\varepsilon_0^M\} = \{a^p\}\ T_o$, $\{\varkappa^M\} = \{\beta^p\}$ T_o and $\Delta T^M = 0$. The residual microstresses were computed for the plain-weave textile beam at the Gaussian center of the elements in the unit-cell. The beam was assumed to be in the x-z plane with unit-cells repeating in the x-direction. Figure 21 shows the thermal stress contours for σ_{xx}, σ_{zz} and τ_{xz}. The composite curing temperature was assumed to be 150ºC above room temperature.

Figure 21. Thermal stress contours in a plain-weave beam for $\Delta T = -150^{\circ}$C.
(a) σ_{xx}; (b) σ_{zz}; (c) τ_{xz}.

<u>4.2 Strength Modeling of Textile Composites</u>

There are many failure criteria or strength theories for unidirectional fiber composites. This, for example, includes maximum stress theory, maximum strain theory and Tsai-Hill theory (Agarwal and Broutman, 1990). Even though failure of a material is a very complex phenomenon, engineering strength theories such as mentioned above have been found to be useful in design. The interpretation of strength values obtained from such theories are different for different materials. For example in metal matrix composites the failure envelope obtained using the above theories will correspond to the initial yield surface (Dvorak et al., 1973). In graphite/epoxy composites the failure theories can be used to predict fiber or matrix failure. In the present study our intent is to explore the possibility of developing such failure criteria for textile composites.

<u>4.2.1 Determination of Composite Failure Envelope</u>

Our approach is similar to that used by Dvorak et al. (1973). A state of homogeneous deformation, corresponding to each of the six macrostrain components, are independently applied to the unit-cell by imposing the boundary conditions explained in Section 2.1. For each case, the various stress components are computed in the elements in the unit-cell—typically at the element Gaussian integration points. These stresses will be referred to as microstresses. Assuming linear elastic behavior, the microstresses can be computed for any arbitrary combination of the macrostrain components. Since we know the macroscale elasticity matrix, we can find a relation between microstresses at a point and any arbitrary state of macrostress as:
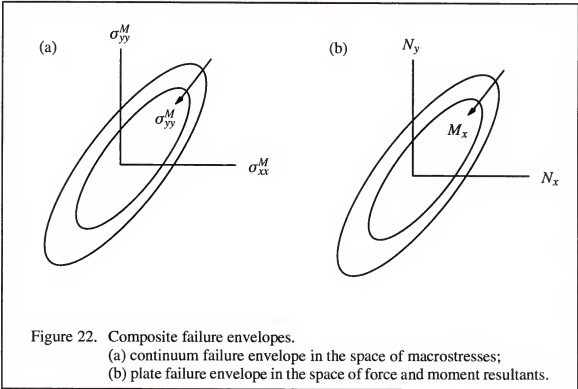
$$\{\sigma\} = [F] \{\sigma^M\} \tag{66}$$

$[F]$ can be considered as a matrix of influence coefficients, which is evaluated at the integration points of all the elements in the unit-cell. We also assume that the failure behavior

of the matrix material and the yarn is known. For instance, let the failure criterion of the matrix be of the form $[H] \{\sigma\}_{\text{matrix}} = 1$. Then the failure criterion for the composite is obtained from Eqn. (66) as $[H][F]\{\sigma^M\} = 1$. The same idea also applies for the yarn. The textile composite is assumed to have failed if there is failure on the microscale in any one of the constituent materials—either matrix or the yarn. By varying the macrostresses using a numerical simulation, failure envelopes can be obtained for the idealized homogeneous material (Fig. 22a). It might be noted that Eqn. (66) can be modified to include the thermal residual stress field in the unit-cell as

$$\{\sigma\} = [F]\{\sigma^M\} - \{\sigma_T\}T_o \tag{67}$$

where $\{\sigma_T\}$ is the matrix of thermal microstresses computed at the element integration point for a unit temperature difference.

Figure 22. Composite failure envelopes.
(a) continuum failure envelope in the space of macrostresses;
(b) plate failure envelope in the space of force and moment resultants.

4.2.2 Effect of Stress Gradients on Strength

The strength analysis for a three-dimensional composite can be extended for thin composites using the plate model. As mentioned in Section 2.2, the macrostresses will not be homogeneous thorough the thickness in such composites. Then the composite failure will be determined by the stress gradients through the thickness, represented by the averaged force resultants (N) and moment resultants (M). The composite failure criterion for the plate model will be of the form:

$$[H][F] \begin{Bmatrix} N \\ M \end{Bmatrix} = 1 \tag{68}$$

Thus the failure envelope of the composite will be in the six-dimensional space of the force resultants and the moment resultants (Fig. 22b). The above procedure was demonstrated using the beam model, for the case of a plain-weave textile composite.

Failure envelope for textile composite beam. For a textile composite beam, the failure envelope is constructed in the space of the three force resultants P, M and V. The textile composite beam is assumed to be in the xz-plane with unit-cells repeating in the x-direction. The unit-cell is discretized with eight-node isoparametric plane strain finite elements. Three linearly independent deformations, as explained in Section 2.3, are applied to the unit-cell: (a) unit axial strain; (b) unit curvature such that transverse shear strain is zero; (c) unit transverse shear strain. For each deformation, from the finite element results, the microstresses σ_{xx}, σ_{zz} and τ_{xz} are computed at the Gaussian center of each element. The microstresses in the ith element for a combination of loads (deformations) are given by:

$$\begin{Bmatrix} \sigma_{xx}^{i} \\ \sigma_{zz}^{i} \\ \tau_{xz}^{i} \end{Bmatrix} = [A^{i}] \begin{Bmatrix} \varepsilon_{0}^{M} \\ \varkappa^{M} \\ \gamma_{0}^{M} \end{Bmatrix} \tag{69}$$

where the each column of $[A^i]$ corresponds to the microstresses for unit deformation. For example, the first column of $[A^i]$ represents the three microstress components in the ith element for unit ε_0^M. We also know that

$$\begin{Bmatrix} \varepsilon_0^M \\ \varkappa^M \\ \gamma_0^M \end{Bmatrix} = [S] \begin{Bmatrix} P \\ M \\ V \end{Bmatrix} \tag{70}$$

where $[S]$ is the beam compliance matrix. From Eqns. (69) and (70) we arrive at an expression analogous to Eqn. (66):

$$\begin{Bmatrix} \sigma_{xx}^i \\ \sigma_{zz}^i \\ \tau_{xz}^i \end{Bmatrix} = [F] \begin{Bmatrix} P \\ M \\ V \end{Bmatrix} \tag{71}$$

where $[F] = [A^i][S]$. The composite is assumed to have failed if there is failure in any one of the finite elements in the unit-cell. Matrix failure is determined by either maximum principal stress or von Mises criteria. Since the yarn is assumed to be transversely isotropic, yarn failure is determined by either maximum strain theory for a unidirectional composite or the Tsai-Wu criteria.

<u>Beam Failure Envelope Results</u>. The strength properties used for the constituent materials in the beam are as follows:

Yarn: $\quad \sigma_L^T$=1725 MPa, σ_L^C=1366 MPa, σ_T^T=42 MPa, σ_T^C=230 MPa, τ_{LT}=95 MPa

Matrix: $\quad \sigma^T$=70 MPa, σ^C=100 MPa

where the superscripts 'T' and 'C' refer to the tensile and compressive strengths respectively. The failure envelopes were developed using two different sets of failure criteria. In the first case maximum principal stress criterion was used to determine the matrix failure and the maximum strain theory for unidirectional fiber composite was used for the yarn. In the second case von Mises criterion was used for the matrix and the Tsai-Wu criteria for the yarn. Both structural (beam) and continuum failure envelopes were developed. As was explained

earlier, in the beam model, periodic BC's were imposed between corresponding nodes on the left and right ends of the unit-cell. In the continuum model, the periodic BC's were in addition imposed between the top and bottom surfaces. The failure envelopes in Figures (23) through (26) were obtained using the first set of failure criteria. Figures (23) and (24) depict the structural failure envelope in the *P-M* space based on yarn and matrix failure respectively. Figures (25) and (26) illustrate similar continuum failure envelopes in the space of the macroscale normal stresses in the *x*- and *z*-directions. As expected, the envelope reduced in size with increasing shear force resultant. If we assume that the beam is made of a homogeneous but orthotropic material with properties as predicted by the continuum model, then one can derive structural failure envelopes from the continuum failure envelopes using simple beam theories. The derived structural failure envelopes are compared with that obtained from direct micromechanical analyses in Figures (27) and (28). One can note that the continuum failure criteria are very conservative for the case of a thin beam. Figures (29) and (30) show similar comparisons for the second set of results obtained using the quadratic failure criteria for the constituent materials.
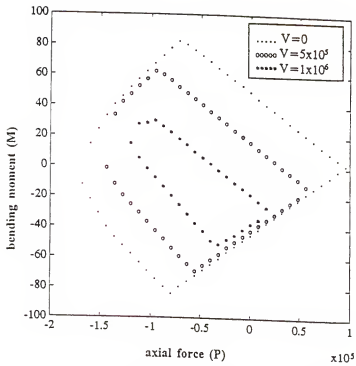
Figure 23. Beam failure envelope based on yarn failure. (maximum strain theory)
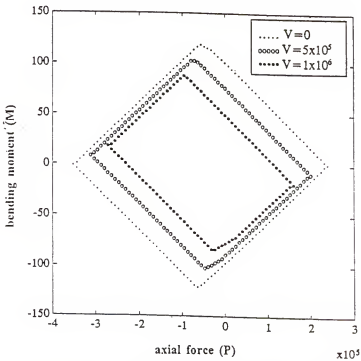
Figure 24. Beam failure envelope based on matrix failure. (maximum principal stress criteria)
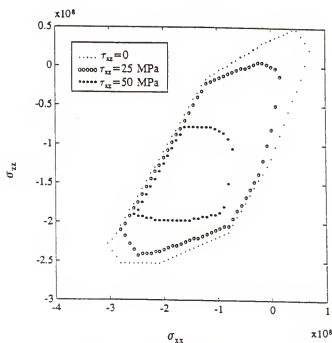
Figure 25. Continuum failure envelope based on yarn failure. (maximum strain theory)
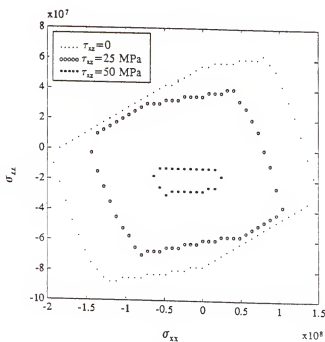

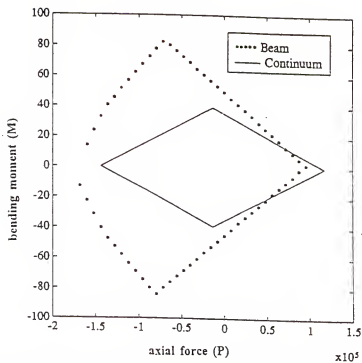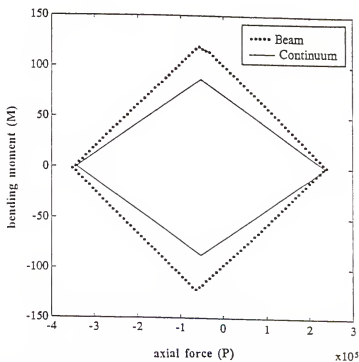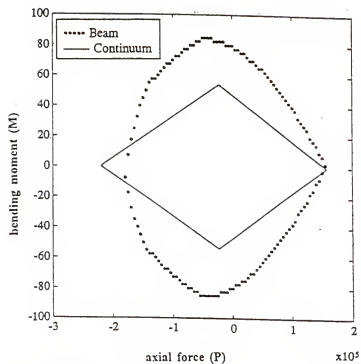Figure 26. Continuum failure envelope based on matrix failure. (maximum principal stress criteria)

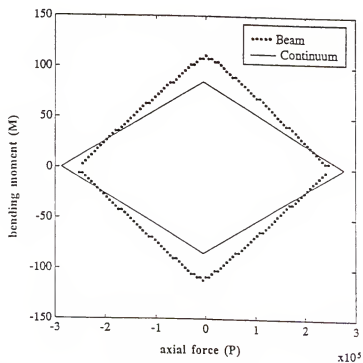Figure 27. Comparison of failure envelopes based on yarn failure. (maximum strain theory)

Figure 28. Comparison of failure envelopes based on matrix failure. (maximum principal stress criteria)

Figure 29. Comparison of failure envelopes based on yarn failure. (Tsai-Wu criteria)

Figure 30. Comparison of failure envelopes based on matrix failure. (von-Mises criteria)

CHAPTER 5
ISSUES IN MICROMECHANICAL MODELING

The complex yarn architectures in textile composites make traditional finite element modeling very difficult. Traditional finite element models assume that the material properties are constant or vary smoothly within an element. In the context of textile composites, it means that the yarn and matrix materials are modeled by separate elements, with common nodes at the yarn-matrix interface. This is indeed preferable because the stresses at the interface can be computed accurately. However meshing the interstitial matrix region becomes time-consuming and difficult. This region which is essentially a collection of multiply-connected matrix pockets, requires a very fine mesh to capture the pocket geometry. Dasgupta et al. (1990) and Whitcomb (1991) presented detailed finite element analyses of the unit-cell for plain-weave architectures. In this chapter, alternative finite element modeling techniques (Marrey and Sankar, 1994) are discussed, which are valid for any yarn architecture. The methods were tested with simple two-dimensional examples, and compared with the displacement fields using traditional finite elements. Some aspects of finite element mesh generation, in the context of textile composites, are also discussed.

5.1 Finite Element Modeling of the Unit-Cell

Traditional finite elements use homogeneous elements, *i.e.*, elements that are comprised of only one material. Two methods to circumvent traditional finite element modeling are described in the following section. The first uses incompatible elements, which employs homogeneous elements for the yarn and matrix, though there is a node mismatch at the yarn-matrix interface. The second method utilizes inhomogeneous elements to model the unit-cell.

5.1.1 Incompatible Elements

The following method is a modification of previously published work on independently modeling substructures with finite elements (Ransom et al., 1993). The matrix and each of the yarns are meshed independently with finite elements. In general, the nodes on the surface of the yarns will not coincide with the matrix nodes on the yarn-matrix interface. In fact, most textile composite unit-cells due to multidirectional reinforcements, contain multiply-connected matrix pockets. These matrix regions require an extremely fine mesh to capture their geometry, whereas the yarns can be modeled with a coarse mesh. This method has therefore two advantages—the first being the relative ease of generating independent meshes for the yarns and the matrix. Secondly, the effective degrees of freedom in the numerical model are reduced, since the yarns are modeled with a coarse mesh.

Figure 31(a) shows an example of a rectangular unit-cell with an ellipsoidal inclusion. The matrix mesh is shown in Fig. 31(b) and the inclusion mesh is shown in Fig. 31(c). The matrix degrees of freedom on the inclusion-matrix interface are denoted as $q_b{}^m$; the matrix degrees of freedom in the interior as $q_i{}^m$ and the inclusion degrees of freedom are denoted as q^y. The total strain energy in the unit-cell is given by

$$U = \frac{1}{2} \lfloor q_b^m \ q_i^m \rfloor \begin{bmatrix} K_{bb}^m & K_{bi}^m \\ K_{ib}^m & K_{ii}^m \end{bmatrix} \begin{Bmatrix} q_b^m \\ q_i^m \end{Bmatrix} \\ + \frac{1}{2} q^{y^T} K^y q^y - q^{y^T} R^y - q_i^{m^T} R_i^m - q_b^{m^T} R_b^m$$

(72)

where K^y is the finite element stiffness for the inclusion; and K^m is the stiffness for the matrix material, which is divided into four sub-matrices. R^y and R^m are the external load vectors in the inclusion and matrix mesh respectively. The matrix degrees of freedom on the boundary are eliminated using the transformation,

$$q_b^m = T q^y$$

(73)

where T is a transformation matrix. By substituting for $q_b{}^m$ in Eqn. (72) and minimizing the strain energy with respect to q^y and $q_i{}^m$, we get the following relation:

$$
\begin{bmatrix} K^y + T^T K_{bb}^m T & T^T K_{bi}^m \\ K_{ib}^m T & K_{ii}^m \end{bmatrix} \begin{Bmatrix} q^y \\ q_i^m \end{Bmatrix} = \begin{Bmatrix} R^y + T^T R_b^m \\ R_i^m \end{Bmatrix} \tag{74}
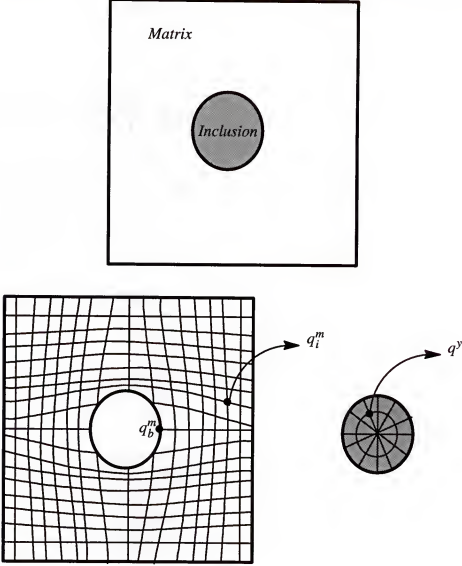$$

Figure 31.   Example to illustrate incompatible elements.
(a) problem to be modeled; (b) matrix mesh; (c) inclusion mesh.

Equation (74) can be solved for q^y and q_i^m, and q_b^m can be recovered from Eqn. (73). The displacement at any point in the unit-cell is obtained by identifying the inclusion or matrix

element enclosing the point, and interpolating the nodal displacements of that element. By repeating this procedure for several representative points, the displacement field within the unit-cell is obtained.

The method was first tested by predicting the displacement field for the unit-cell of a unidirectional composite subject to uniaxial tension. Due to symmetry of the unit-cell, only one-quarter of the unit-cell was modeled. The boundary conditions imposed required the edges of the unit-cell to remain straight after deformation (Fig. 32a). The initial mesh for the problem is shown in Fig. 32(b). The node mismatch at the inclusion-matrix interface can be observed in the figure. Eight-node isoparametric elements were used to model the fiber and matrix—24 elements were used for the fiber and 98 elements for the matrix. The deformed incompatible element configuration is shown in Fig. 32(c). The results were compared with conventional finite element results by plotting the displacement fields for both cases on a background 25x25 mesh (Fig. 32d). It was found that the incompatible element displacement field was identical to that using traditional elements. Only one set of displacements are visible in Fig. 32(d), because the displacement fields exactly overlapped each other.

The procedure to determine the background mesh displacement field is illustrated in Fig. 33. For a given point in the background mesh (Fig. 33a), the corresponding incompatible element containing the point is determined (Fig. 33b). The displacement for the mesh point is obtained as the interpolation of nodal displacements of the found incompatible element (Fig. 33c). A similar procedure is followed to compute the background mesh displacements using conventional elements. The method was also tested by modeling the transverse shear of a unidirectional composite (Fig. 34). In this case, one-half of the unit-cell was modeled and the displacements are shown for a background 20x20 mesh. In both examples, it was found that the displacement fields using incompatible elements and conventional elements were identical. A discontinuity in strains in the vicinity of the fiber-matrix interface was observed in both the examples.
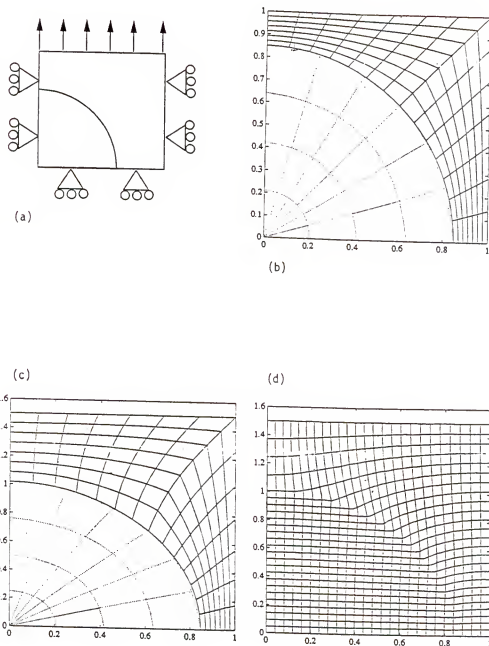
Figure 32.   Unidirectional composite subjected to uniaxial tension.
(a) boundary conditions; (b) initial mesh using incompatible elements;
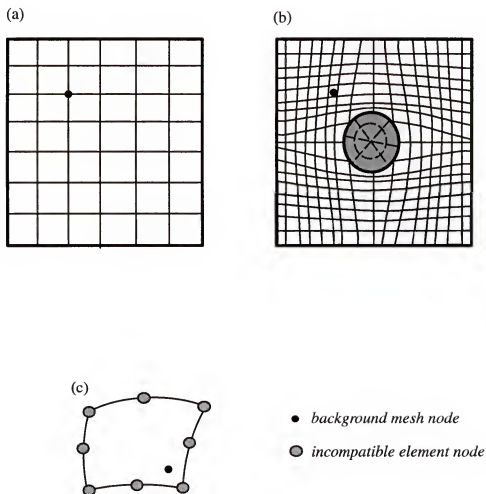(c) deformed mesh; (e) deformed background mesh.

Figure 33. Calculating displacement field for the background mesh.
(a) background mesh showing node whose displacements are to be
calculated; (b) incompatible element mesh; (c) matrix element
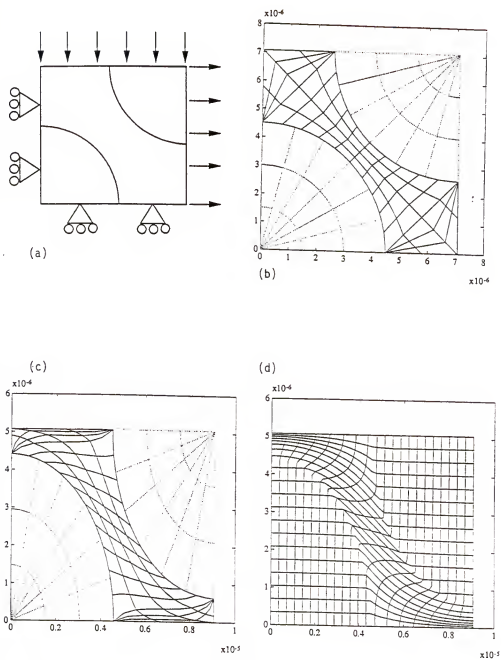containing the background mesh node.

Figure 34. Unidirectional composite subjected to transverse shear.
(a) boundary conditions; (b) initial mesh using incompatible elements;
(c) deformed mesh; (e) deformed background mesh.

5.1.2 Inhomogeneous Elements (Averaged Gaussian Integration)

By inhomogeneous elements, we mean finite elements which are comprised of more than one material. Inhomogeneous elements in micromechanical analyses were studied in detail by Foye (1993). The advantage of using inhomogeneous elements is that mesh generation is very simple. For instance a rectangular domain can be discretized into uniform rectangular or triangular elements, without taking into consideration the constituent material geometry. The stiffness matrix of inhomogeneous elements represent smeared properties of the constituent phases determined by the numerical integration scheme. Thus the solution will be approximate in the interface regions. Foye has developed a modified method to evaluate the stiffness matrix of inhomogeneous elements called Replacement Elements, which predict better stresses than conventional inhomogeneous elements. The following details the procedure to use inhomogeneous elements for micromechanical analysis.

The unit-cell is divided into uniform rectangular hexahedral elements as shown in Fig. 35. In general these elements will be inhomogeneous. The stiffness matrix (K^e) for an inhomogeneous element is formulated as:

$$
\begin{aligned}
K^e &= \int_{V^e} B^T C B \; dV^e \\
&= \int_{-1}^{+1} \int_{-1}^{+1} \int_{-1}^{+1} B^T C B \; |J| \; d\xi d\eta d\zeta \\
&= \sum_{i=1}^{N} \sum_{j=1}^{N} \sum_{k=1}^{N} W_i W_j W_k \; B^T C(\xi,\eta,\zeta) \; B |J|
\end{aligned}
\tag{75}
$$

where V^e is the domain of the element, B is the strain-displacement transformation matrix, C is the elasticity matrix, N is the number of Gauss points used for integration, W is the Gaussian integration weight factor and $|J|$ is the determinant of the Jacobian. The material property at each Gauss point (ξ,η,ζ) is determined, and the corresponding elasticity matrix

is used to perform the volume integration. The element stiffness matrix will thus represent the averaged properties of the constituent materials in that element.
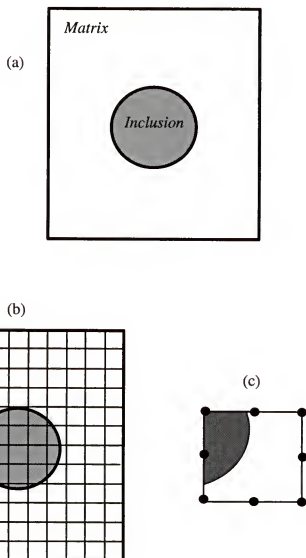

Figure 35. Discretizing a domain using inhomogeneous finite elements.
(a) problem to be modeled; (b) inhomogeneous finite element mesh;
(c) inhomogeneous finite element.

The approach was implemented by writing a code to identify the material property of an arbitrary Gauss point. The inclusion geometry was defined by a coarse finite element mesh. If the Gauss point fell within any of the inclusion elements—the material property of the point was identified as that of inclusion. Otherwise the material property of the point was identified as matrix. The algorithm to determine the element belonging to the Gauss point is explained in the following section. The results obtained by using the approach to the uniaxial tension of a unidirectional composite are shown in Fig. 36(a). The displacements were in agreement with those obtained using homogeneous elements (Fig. 36b).

The problem with inhomogeneous elements is that they cannot represent the jump in strains that can occur at the yarn-matrix interface. In fact there are three strain components that can be discontinuous at the interface, but the corresponding stresses must be continuous. Such a behavior cannot be represented by inhomogeneous elements which assume a continuous strain fields within the element. This problem can be resolved by decomposing the displacement field into two parts: a displacement field q_1 that produces a strain field continuous everywhere in the unit-cell, and the second one q_2 that has a strain discontinuity at the yarn-matrix interface. The field q_2 can be assumed to be such that the displacements are identically equal to zero everywhere in the matrix and at the interface, and exist only in the interior of the inclusions. Thus one can use inhomogeneous elements for solving the first set of displacements. The second set of displacements exists only in the inclusions, and they can be solved by discretizing only the inclusion. However the issue is determining the decomposition $q = q_1 + q_2$. The condition for the decomposition is that the jump in interfacial stresses should be equal and opposite in the two problems, since the interfacial stresses are continuous in the given problem.
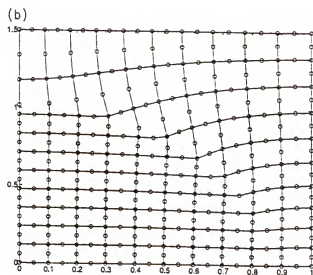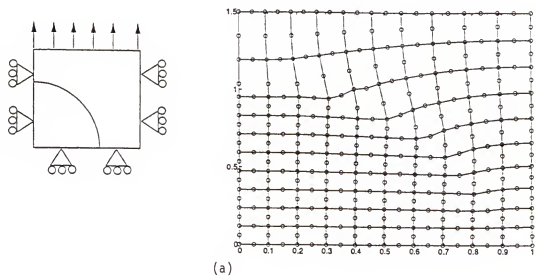
Figure 36. Displacement field for uniaxial tension of a unidirectional composite.
(a) inhomogeneous elements; (b) homogeneous elements.

Point location algorithm. In the context of a textile composite problem, the material property code of a point is obtained as follows. The yarn (inclusion) volume is discretized into eight-node hexahedral isoparametric finite elements as shown in Fig. 37. The finite elements are shaped as triangular prisms (a face of the hexahedron is collapsed to an edge). An iterative algorithm is used to determine whether the point (whose material property is to be determined) is contained within the volume of a given element. If not, the procedure is repeated for all the elements in the yarn. If the point does not belong to any of the yarns, it is designated as a matrix point. If the point belongs to a yarn element, the local yarn direction is computed as the direction of the line along the length of the prismatic element.
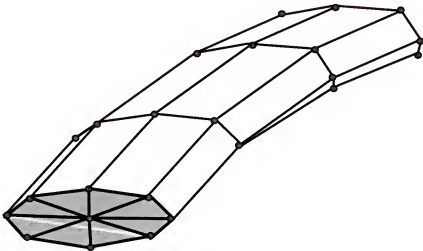

Figure 37. Finite element mesh for a yarn.

The algorithm to determine if a given point is contained within the volume of a finite element is explained below. The procedure is explained for the two-dimensional case, and can be easily extended to a three-dimensional problem.
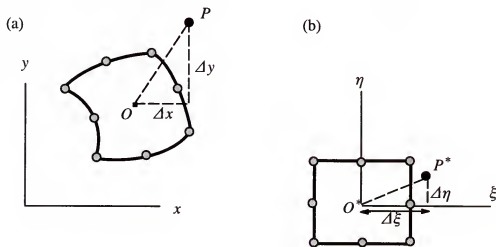
Figure 38. Finite element in:
           (a) xy–coordinate system (b) natural coordinate system.

Let the point, whose material property is to be determined, be P with coordinates (x,y). It is required to determine whether the point P is contained within the area of the eight-node isoparametric element as shown in Fig. 38(a). The element is mapped into its natural coordinate system (Fig. 38b). Similarly, point P is mapped to P^* in the element natural coordinate system. The element in the (ξ,η) natural coordinate system is a square of length two units with edges parallel to the $\xi\eta$-axes, such that the center of the square O^* coincides with the natural coordinate origin. This means that we need to find whether the point P^* is contained within the given square. This is possible if we know the natural coordinates of point P^*. However there does not exist a transformation from the xy-coordinate system to the natural coordinate system. The reverse transformation exists as given below:

$$x(\xi,\eta) = \sum_{i=1}^{8} N_i(\xi,\eta)\ x_i$$

$$y(\xi,\eta) = \sum_{i=1}^{8} N_i(\xi,\eta)\ y_i \qquad (76)$$

where N_i denotes the shape function, and (x_i, y_i) represents the xy-coordinates for the ith node. Therefore we use an iterative procedure to determine the natural coordinates of P^*.

We substitute $\xi=0$ and $\eta=0$ in Eqn. (76), and determine the xy-coordinates of point O (corresponding to point O^* in the natural coordinate system). The point O will not, in general, coincide with P. Then the error, $i.e.$, the difference in the x- and y-coordinates between points P and O is calculated as Δx and Δy respectively. Also since the x- and y-coordinates are functions of the natural coordinates, Δx and Δy may be expressed as:

$$\Delta x = \frac{\partial x}{\partial \xi}\Delta\xi + \frac{\partial x}{\partial \eta}\Delta\eta$$

$$\Delta y = \frac{\partial y}{\partial \xi}\Delta\xi + \frac{\partial y}{\partial \eta}\Delta\eta \qquad (77)$$

Equation (77) may be rewritten in matrix form as follows:

$$\left\{ \begin{array}{c} \Delta x \\ \Delta y \end{array} \right\} = \begin{bmatrix} \dfrac{\partial x}{\partial \xi} & \dfrac{\partial x}{\partial \eta} \\ \dfrac{\partial y}{\partial \xi} & \dfrac{\partial y}{\partial \eta} \end{bmatrix} \left\{ \begin{array}{c} \Delta\xi \\ \Delta\eta \end{array} \right\} \qquad (78)$$

$$\left\{ \begin{array}{c} \Delta x \\ \Delta y \end{array} \right\} = [J(\xi,\eta)]^T \left\{ \begin{array}{c} \Delta\xi \\ \Delta\eta \end{array} \right\} \qquad (79)$$

where $[J(\xi,\eta)]$ is the Jacobian at (ξ,η). The Jacobian is computed using the following equation:

$$[J] = \begin{bmatrix} \dfrac{\partial N_1}{\partial \xi} & \dfrac{\partial N_2}{\partial \xi} & \cdots & \dfrac{\partial N_8}{\partial \xi} \\ \dfrac{\partial N_1}{\partial \eta} & \dfrac{\partial N_2}{\partial \eta} & \cdots & \dfrac{\partial N_8}{\partial \eta} \end{bmatrix} \left\{ \begin{array}{cc} x_1 & y_1 \\ x_2 & y_2 \\ \vdots & \vdots \\ x_8 & y_8 \end{array} \right\} \qquad (80)$$

Knowing the Jacobian, $\Delta\xi$ and $\Delta\eta$ can be evaluated from Eqn. (79) as:

$$\begin{Bmatrix} \Delta\xi \\ \Delta\eta \end{Bmatrix} = [J(\xi,\eta)]^{-T} \begin{Bmatrix} \Delta x \\ \Delta y \end{Bmatrix} \tag{81}$$

The parameters $\Delta\xi$ and $\Delta\eta$ are the corrections to be applied to the coordinates of point O^* to determine the coordinates of point P^*. As a check, the natural coordinates of point P^* is then transformed to its xy-coordinates using Eqn. (76), and compared with the given coordinates of point P. The procedure is repeated if the difference in coordinates is above a prescribed tolerance.

5.1.3 Periodic Boundary Conditions

The unit-cell is the smallest volume element in the composite which is representative of the yarn architecture. The yarn architecture in the composite is generally periodic, and the unit-cell contains one repeat of the yarn pattern. Thus the composite structure can be formed by assembling the unit-cell in all three dimensions. When the composite is subject to any arbitrary load, the microstresses and displacement gradients will be continuous across the faces of the unit-cell. Continuity of microstresses requires that the tractions be equal and opposite at corresponding points on opposite faces of the unit-cell. Also the displacements between corresponding nodes on opposite faces of the unit-cell will differ only by a constant.

Multipoint constraint elements. The periodic boundary conditions (traction and displacement boundary conditions) can be implemented using multipoint constraint elements, which are based on the principle of Lagrange multipliers. The finite element formulation with multipoint constraint elements will be of the form:

$$\begin{bmatrix} K & C \\ C^T & 0 \end{bmatrix} \begin{Bmatrix} D \\ \lambda \end{Bmatrix} = \begin{Bmatrix} R \\ Q \end{Bmatrix} \tag{82}$$

where $\{\lambda\}$ is the matrix of Lagrange multipliers (Cook et al., 1989). However this method requires large storage for the stiffness matrix, due to the degrees of freedom contributed by the constraint elements (λ_i). Also the resulting stiffness matrix will not be positive definite, and the matrix bandwidth will be very large.
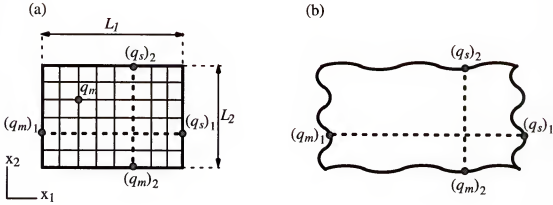
Figure 39. Two-dimensional example to illustrate the use of transformation equations.
(a) initial finite element mesh of unit-cell showing some of the master
and slave degrees of freedom; (b) deformed mesh.

Transformation equations. The following section explains an alternative method to enforce the periodic boundary conditions. The method is explained for the two-dimensional case, and can easily be extended for the three-dimensional problem. Consider a finite element mesh of a unit-cell (Fig. 39a), where the periodic boundary conditions are to be implemented between the left and right edges, and the top and bottom edges. Assume that each node has only one degree of freedom (d.o.f). The nodal degrees of freedom on the left and bottom edges (except the prescribed d.o.f's) are designated as "master" degrees of freedom q_m, and those on the right and top edges as "slave" degrees of freedom q_s. The nodal degrees of freedom in the mesh interior are also classified as master degrees of freedom. There may arise a situation where the d.o.f for the corner node at $x_1=0$, $x_2 = 0$ is not prescribed. In that case, it is designated as a master node with two slave nodes, whose coordinates are given by ($x_1=0$, $x_2 = L_2$) and ($x_1=L_1$, $x_2 = 0$). Thus a master d.o.f may have zero, one or two slave d.o.f's depending on its coordinates.

The slave d.o.f's are transformed to master d.o.f's by the transformation:

$$q_s = A q_m + \Delta q_s \tag{83}$$

where A is a transformation matrix such that $A_{ij} = \delta_{c(i)j}$, and δ denotes the Kronecker delta. "c" is an integer function such that for the ith slave d.o.f, $c(i)$ is the corresponding master d.o.f. Equation (83) can be rewritten as,

$$
\begin{aligned}
(q_s)_i &= \sum_j A_{ij}(q_m)_j + (\Delta q_s)_i \\
&= \sum_j \delta_{c(i)j}(q_m)_j + (\Delta q_s)_i \\
&= (q_m)_{c(i)} + (\Delta q_s)_i
\end{aligned}
\tag{84}
$$

$(\Delta q_s)_i$ is the displacement difference to be imposed between the ith slave d.o.f $(q_s)_i$ and its corresponding master d.o.f, $(q_m)_{c(i)}$. The strain energy in the unit-cell is evaluated as,

$$
\begin{aligned}
U = \ & \frac{1}{2} \begin{Bmatrix} q_m \\ q_s \end{Bmatrix}^T \begin{bmatrix} K_{mm} & K_{ms} \\ K_{sm} & K_{ss} \end{bmatrix} \begin{Bmatrix} q_m \\ q_s \end{Bmatrix} \\
& + \lambda^T(q_s - A q_m - \Delta q_s) - q_s^T R_s - q_m^T R_m
\end{aligned}
\tag{85}
$$

where λ is the matrix of Lagrange multipliers; R_s and R_m represent the external force vectors for the slave and master d.o.f's. By minimizing the strain energy with respect to the variables q_m, q_s and λ we get:

$$
\begin{bmatrix} K_{mm} & K_{ms} & -A^T \\ K_{sm} & K_{ss} & I \\ -A & I & 0 \end{bmatrix} \begin{Bmatrix} q_m \\ q_s \\ \lambda \end{Bmatrix} = \begin{Bmatrix} R_m \\ R_s \\ \Delta q_s \end{Bmatrix}
\tag{86}
$$

Eliminating q_s and λ from Eqn. (86), we arrive at the expression :

$$K^* q_m = R^* \tag{87}$$

where

$$
\begin{aligned}
K^* &= [K_{mm} + A^T K_{ss} A + A^T K_{sm} + K_{ms} A] \\
R^* &= R_m + A^T R_s - [K_{ms} + A^T K_{ss}] \Delta q_s
\end{aligned}
\tag{88}
$$

Equation (87) can be solved for q_m; and q_s recovered from Eqn. (83). Thus the number of unknowns in the linear equation solver are reduced, and also the resulting stiffness matrix (K^*) is positive-definite.

5.2 Mesh Generation

Currently approximate methods such as averaged Gaussian integration, Selective Averaging Method and Isostrain Method are popular because of their ease of computation and requirement of minimum computer storage and time. However the advancements in computer hardware and computational technology will make it possible to use a large number of degrees of freedom for micromechanical analysis. Then there will be a need for mesh generation techniques for creating homogeneous elements in a unit-cell. In the following we describe two methods for discretizing the unit-cell with homogeneous elements.

5.2.1 Node Migration Method

The unit-cell is meshed with tetrahedral solid elements in an arbitrary fashion. This will be called the primitive mesh. The elements are identified as homogeneous or inhomogeneous. Then the nodes of the inhomogeneous elements are moved to the interface by using an heuristic algorithm. In each inhomogeneous element, the node closest to the interface is allowed to migrate to the interface first. After each cycle, some elements will transform into homogeneous elements. Then the process is repeated until all the elements become homogeneous. The mesh thus generated is called the intermediate mesh.

The intermediate mesh will have some elements distorted due to node migration. This distortion can be removed by subjecting the mesh to an annealing process, by which the distortions concentrated near the interfaces are distributed among other elements also. An example of this method is depicted in Fig. 40. The purpose here is to discretize a square unit-cell containing two circular inclusions. The figure shows the initial mesh containing

uniform square elements, the intermediate mesh of homogeneous elements and the annealed mesh.
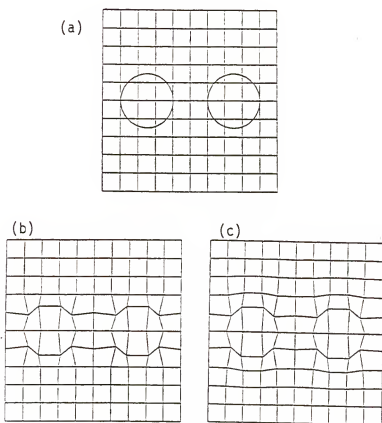

Figure 40. Example problem for node migration method.
            (a) primitive mesh; (b) intermediate mesh; (c) annealed mesh.

5.2.2 Modified Node Migration Method

In this method an initial mesh is created as in the previous method. The elements are divided into three groups: homogeneous matrix elements, homogeneous yarn elements and inhomogeneous elements which contain both matrix and yarn. Then the inhomogeneous elements are redesignated as matrix elements, thus leaving only two kinds of elements. We will call this as the intermediate mesh. Thus the finite element representation of the yarn will be smaller than the actual yarn, *i.e.,* the yarn mesh will be fully contained within the actual yarn. Then the nodes on the yarn-matrix interface in the intermediate mesh are allowed to migrate to the nearest point on the actual yarn-matrix interface. As before a three-dimensional finite element program with fictitious material properties is used in this step to obtain an annealed mesh. An example of the final mesh for a square unit-cell with two inclusions in the shape of a quarter-circle is shown in Fig. 41.
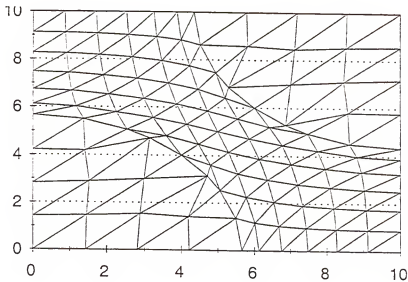

Figure 41. Annealed mesh using modified node migration method.

CHAPTER 6
CONCLUSIONS AND SUGGESTIONS FOR FUTURE WORK

The previous chapters presented some of the aspects involved in the modeling of textile structural composites. Micromechanical analyses were developed to predict the three-dimensional elastic constants and CTE's for textile composite materials. The effect of stress gradients in thin textile composites was highlighted, and consequently, an independent micromechanical analysis was developed for such composites. The issues involved in modeling a thin textile composite were demonstrated by first modeling the composite as a beam and then as a plate. Two codes called $\mu TE\chi$-10 and $\mu TE\chi$-20 were developed in FORTRAN 77, which implemented the finite element procedure presented in Chapter 2, and the SAM procedure presented in Chapter 3 respectively. The predicted macroscale thermo-elastic constants compared very well with existing models for textile composite materials.

The finite element analysis and SAM procedures assume that the unit-cell of the composite is shaped as a rectangular hexahedron. Both analyses can be easily modified for other unit-cell geometries. For example, in the finite element procedure, the relations for the periodic boundary conditions will change based on the unit-cell geometry. However the assumption, that the unit-cell is rectangular, limited the textile composite examples for which the above codes can be implemented. For instance, the unit-cell for a braided composite is hexahedral with the included angle between the edges equal to the braid angle. The braid angle, in general, will not be equal to a right angle. Thus the effective composite properties could be computed only for woven architectures, where the unit-cell is a rectangular hexahedron.

A considerable amount of time was invested in developing mesh generation algorithms and alternative finite element procedures, in the context of modeling textile composites. Some of these ideas are presented in Chapter 5. The mesh generation algorithms such as the node migration method were very effective for two-dimensional examples. However for the three-dimensional case, some of the elements near the interface collapsed to create degenerate and skewed elements. Further, extremely small tetrahedral elements were required to capture the interstitial matrix geometry. Computer storage and CPU time limitations made the use of such a finite element mesh impractical. Initially multipoint constraint elements were used to impose periodic boundary conditions in $\mu TE\chi$-10. To reduce computer storage, the transformation method (for periodic boundary conditions) and the skyline solver (Bathe, 1982) were incorporated in the finite element code. Further reduction in computer storage can be realized by using sparse matrix solvers instead of the skyline solver.

The averaged Gaussian integration technique was used to compute the inhomogeneous element stiffness matrix in $\mu TE\chi$-10. The inhomogeneous element averages the properties of the constituent materials in the element, and assumes that the strain distribution is continuous within the element. Consequently, the inhomogeneous element cannot capture the discontinuity in strains across the yarn-matrix interface. Thus the corresponding microstresses computed in the vicinity of the interface will be inaccurate. The accuracy of the microstresses may be improved by refining the (inhomogeneous element) mesh, but that would greatly increase the degrees of freedom in the numerical model. This emphasizes the need for effective finite element preprocessing codes for meshing the unit-cell of the textile composite with homogenous elements. It will also be useful to interface the finite element results with suitable graphics software. This will enable the user to get a feel for the problem by directly visualizing the unit-cell deformed configurations, and the microstress/microstrain distributions within the unit-cell.

Chapter 4 presented failure envelope results for a plain-weave textile beam. Implicit to the procedure for determining the failure envelope, was the assumption that microscopic failure in the unit-cell translated to macroscopic failure of the composite. The procedure is simplistic and conservative, but yet of use to a structural designer. More work remains to be done in obtaining results for failure envelopes using the strength models for textile composite continuum and for a composite plate, as explained in Chapter 4. An issue which this study, due to time limitations, does not address is parametric analyses to study the effect of changing constituent material properties and fiber volume fraction on composite properties. Both the finite element analysis and SAM can be easily extended for other macroscopic composite properties such as thermal conductivities, electro-magnetic properties and so on.

REFERENCES

Agarwal, D. A., and Broutman, L. J., 1990, *Analysis and Performance of Fiber Composites*, John Wiley and Sons, New York.

Bathe, K. J., 1982, *Finite Element Procedures in Engineering Analysis*, Prentice-Hall, Englewood Cliffs, New Jersey.

Chou, T. W., and Ko, F. K., 1989, *Textile Structural Composites*, Composite Materials Series – Vol. 3, Elsevier, New York.

Christensen, R., 1990, "A critical evaluation for a class of micromechanics models", *Journal of the Mechanics and Physics of Solids*, Vol. 38, No. 3, pp. 379-404

Cook, R. D., Malkus, D. S., and Plesha, M. E., 1989, *Concepts and Applications of Finite Element Analysis*, John Wiley and Sons, Third Edition, New York.

Cox, B. N., Carter, W. C., and Fleck, N. A., 1994, "A binary model of textile composites – I. Formulation", *Acta metallurgica et materialia,* Vol. 42, No. 10, pp. 3463-3479.

Crane, R. M., and Camponeschi, E. T., 1986, "Experimental and analytical characterization of multidimensionally braided graphite/epoxy composites", *Experimental Mechanics,* September, pp. 259-266.

Dasgupta, A., Bhandarkar, S., Pecht, M., and Barkar, D., 1990, "Thermo-elastic properties of woven–fabric composites using homogenization techniques", *Proceedings of the American Society for Composites. Fifth Technical Conference.*, Lansing, Michigan, pp. 1001-1010.

Dvorak, G. J., Rao, M. S. M., and Tarn, J. Q., 1973, "Yielding in unidirectional composites under external loads and temperature Changes", *Journal of Composite Materials*, Vol.7, pp. 194-216.

Foye, R. L., 1993, "Approximating the stress field within the unit cell of a fabric reinforced composite using replacement elements", *NASA CR-191422.*

Halpin, J. C., and Tsai, S. W., June 1969, "Effects of Environmental Factors on Composite Materials", *AFML-TR-67-423.*

Hashin, Z., 1962, "The elastic moduli of heterogenous materials", *Journal of Applied Mechanics*, pp. 143-150.

Ishikawa, T., and Chou, T. W., 1982a, "Elastic behavior of woven hybrid composites", *Journal of Composite Materials*, Vol. 16, pp. 2-19.

Ishikawa, T., and Chou, T. W., 1982b, "Stiffness and strength behavior of woven fabric composites", *Journal of Materials Science*, Vol. 17, pp. 3211-3220.

Ishikawa, T., and Chou, T. W., 1983a, "One-dimensional micromechanical analysis of woven fabric composites", *AIAA Journal*, Vol. 21, pp. 1714-1721.

Ishikawa, T., and Chou, T. W., 1983b, "In-plane thermal expansion and thermal bending coefficients of fabric composites", *Journal of Composite Materials*, Vol. 17, pp. 92-104.

Ishikawa, T., and Chou, T. W., 1983c, "Thermoelastic analysis of hybrid fabric composites", *Journal of Materials Science*, Vol. 18, pp. 2260-2268.

Ma, C. L., Yang, J. M., and Chou, T. W., 1986, "Elastic stiffness of three-dimensional braided textile structural composites", *Composite Materials: Testing and Design (Seventh Conference),* ASTM STP 893, pp. 404-421.

Marrey, R. V., and Sankar, B. V., 1993a, "Stress gradient effects on stiffness and strength of textile structural composites", *Composite Materials and Structures, 1993 ASME Winter Annual Meeting,* New Orleans, Louisiana, AD-Vol. 37/AMD-Vol. 179, pp. 133-148.

Marrey, R. V., and Sankar, B. V., 1993b, "Thermo-mechanical properties of and residual stresses in textile structural composites", *Proceedings of the American Society for Composites. VIII Tech. Conference,* Cleveland, Ohio, pp. 499-508.

Marrey, R. V., and Sankar, B. V., 1994, "Evaluation of finite element micromechanical analysis methods for textile composites", *Proceedings of the 1994 ASME Winter Annual Meeting,* 94-WA/AERO-1, Chicago, Illinois, Nov. 6-11.

Naik, R. A., 1994, "Analysis of woven and braided fabric reinforced composites", *NASA CR-194930.*

Raju, I. S., Foye, R. L., and Avva, V. S., 1990, "A review of analytical methods for fabric and textile composites", *Proceedings of the Indo-U.S. Workshop on Composite Materials for Aerospace Applications,* Bangalore, India, Part I, pp. 129-159.

Ransom, J. B., McCleary, S. L., and Aminpour, M. A., 1993, "A new interface element for connecting independently modeled substructures", *34th Structures, Structural Dynamics and Materials Conference,* LaJolla, California, pp. 1693-1703.

Sankar, B. V., and Marrey, R. V., 1992, "A unit-cell analysis for predicting the [A], [B] and [D] matrices of a textile composite plate", *Technical Note CAC-TN-92-01, Center for Advanced Composites. University of Florida.*

Sankar, B. V., and Marrey, R. V., 1993a, "Micromechanical models for textile structural composites", *Proceedings of 13th Army Symposium on Solid Mechanics,* Plymouth, Massachusetts, pp. 189-200.

Sankar, B. V., and Marrey, R. V., 1993b, "A unit-cell model of textile composite beams for predicting stiffness properties", *Composites Science and Technology*, Vol. 49, pp. 61-69.

Sharma, S. K., and Sankar, B. V., 1995, "Effects of through-the-thickness stitching on impact and interlaminar fracture properties of textile graphite/epoxy laminates", *NASA CR-195042.*

Whitcomb, J. D., 1991, "Three-dimensional stress analysis of plain weave composites", *Composite Materials Fatigue and Fracture (Third Volume)*, ASTM STP 1110, pp. 417-438.

Whitney, J. M., 1973, "Shear correction factors for orthotropic laminates under static load", *Journal of Applied Mechanics*, Vol. 40, pp. 302-304.

Whitney, T. J., and Chou, T. W., 1989, "Modeling of 3-D angle-interlock textile composite structures", *Journal of Composite Materials*, Vol. 23-9, September, pp. 890-911.

Yang, J. M., Ma, C. L., and Chou, T. W., 1986, "Fiber inclination model of three-dimensional textile composite structures", *Journal of Composite Materials*, Vol. 20-5, pp. 472-484.

Yoshino, T., and Ohtsuka, T., 1982, "Inner stress analysis of plane woven fiber reinforced plastic laminates", *Bulletin of the JSME*, Vol. 25-202, pp. 485-492.

BIOGRAPHICAL SKETCH

Ramesh V. Marrey was born on October 13, 1966, at Kakinada, India. He received the degree of Bachelor of Technology in Mechanical Engineering on July 1988, from the Indian Institute of Technology, Madras, India. He then enrolled in the Department of Aerospace Engineering, Mechanics and Engineering Science at the University of Florida. Upon completing his M.S. in engineering mechanics on August 1991, he was admitted to the doctoral program in the same department. He received a Ph. D. degree in engineering mechanics on August 1995.
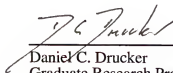
I certify that I have read this study and that in my opinion it conforms to acceptable standards of scholarly presentation and is fully adequate, in scope and quality, as a dissertation for the degree of Doctor of Philosophy.

Bhavani V. Sankar, Chairperson
Professor of Aerospace Engineering,
    Mechanics and Engineering Science

I certify that I have read this study and that in my opinion it conforms to acceptable standards of scholarly presentation and is fully adequate, in scope and quality, as a dissertation for the degree of Doctor of Philosophy.

Nicolae D. Cristescu
Graduate Research Professor
    of Aerospace Engineering, Mechanics
    and Engineering Science

I certify that I have read this study and that in my opinion it conforms to acceptable standards of scholarly presentation and is fully adequate, in scope and quality, as a dissertation for the degree of Doctor of Philosophy.
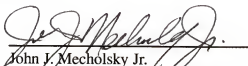
Daniel C. Drucker
Graduate Research Professor Emeritus
    of Aerospace Engineering, Mechanics
    and Engineering Science

I certify that I have read this study and that in my opinion it conforms to acceptable standards of scholarly presentation and is fully adequate, in scope and quality, as a dissertation for the degree of Doctor of Philosophy.

Peter G. Ifju
Assistant Professor of Aerospace
Engineering, Mechanics and
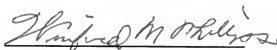Engineering Science

I certify that I have read this study and that in my opinion it conforms to acceptable standards of scholarly presentation and is fully adequate, in scope and quality, as a dissertation for the degree of Doctor of Philosophy.

John J. Mecholsky Jr.
Professor of Materials Science and
Engineering

This dissertation was submitted to the Graduate Faculty of the College of Engineering and to the Graduate School and was accepted as partial fulfillment of the requirements for the degree of Doctor of Philosophy.

August 1995

Winfred M. Phillips
Dean, College of Engineering

Karen A. Holbrook
Dean, Graduate School